Journal of Petrology, 2025, **66**, egaf007
https://doi.org/10.1093/petrology/egaf007
ADVANCE ACCESS PUBLICATION DATE 31 JANUARY 2025
Original Manuscript

Granitoid Metasomatism and Giant Quartz Vein Formation by Mineral Replacement: Insights from the Canigó Massif, Eastern Pyrenees

ELOI GONZÁLEZ-ESVERTIT[1,2,3,*], ÀNGELS CANALS[2], CLAUDIA PRIETO-TORRELL[2,3], PAUL D. BONS[4,5], MARIA-GEMA LLORENS[1], JOSEP MARIA CASAS[6], CARMEN AGUILAR[2], JOYCE NEILSON[7], MARLINA A. ELBURG[8] and ENRIQUE GOMEZ-RIVAS[2]

[1]Geosciences Barcelona, GEO3BCN-CSIC, Lluís Solé i Sabarís s/n, 08028 Barcelona, Spain
[2]Departament de Mineralogia, Petrologia i Geologia Aplicada, Facultat de Ciències de la Terra, Universitat de Barcelona, Martí i Franquès s/n, 08028 Barcelona, Spain
[3]Institut de Recerca Geomodels, Facultat de Ciències de la Terra, Universitat de Barcelona, Martí i Franquès s/n, 08028 Barcelona, Spain
[4]Department of Geosciences, Tübingen University, Schnarrenbergstrasse 94-96, 82076 Tübingen, Germany
[5]School of Earth Science and Resources, China University of Geosciences (Beijing), 110083 Beijing, China
[6]Departament de Dinàmica de la Terra i l'Oceà, Facultat de Ciències de la Terra, Universitat de Barcelona, Martí i Franquès s/n, 08028 Barcelona, Spain
[7]School of Geosciences, King's College, University of Aberdeen, Meston Building, AB24 3UE Aberdeen, United Kingdom
[8]Department of Geology, University of Johannesburg, Auckland Park, P.O. Box 524, 2006 Johannesburg, South Africa

[*]Corresponding author. +34 931027584, e.gonzalez-esvertit@ub.edu
[†]Handling Editor: Prof. Valentin Troll

Metasomatism is a ubiquitous process in the Earth's crust, exerting major controls on fluid, heat and mass transfer and rock deformation, and is commonly constituted by mineral replacement reactions. Different types of metasomatism may coexist and/or successively conceal each other in a given area. Deciphering the geochemical behaviour, regional extent and mineralogical changes of multi-stage metasomatism can be difficult because of the overprinting of successive events and their frequent relationship with deformation. Here, we investigate granitoid metasomatism, namely silicification, feldspathisation and sericitisation, in the Variscan basement rocks of the Canigó Massif (Eastern Pyrenees, SW Europe), which is spatially related to Giant Quartz Veins (GQVs) tens of metres wide and several kilometres long. Unaltered and altered granitic orthogneisses derived from Ordovician intrusives and late-Variscan granitoids, as well as GQV occurrences, are studied across scales through structural and textural characterisation, whole-rock geochemistry and Electron Backscatter Diffraction (EBSD). Geochemical analyses are further compared with a new database including more than 600 unaltered granite and orthogneiss samples from the Pyrenees and the Catalan Coastal Ranges (SW European Variscan Belt). Results show that silicification, the dominant metasomatic process, was related to regional-scale shear zones and contributed to form GQVs through mineral replacement. This is confirmed at the macro- (km), meso- (m–cm) and micro-scale (μm) by relict fabrics, mineral phases and structural features of the precursor rocks within veins, by a progressive depletion of all major and trace elements, except silica, in rocks sampled along decreasing distances from GQV outcrops, and by the localisation of mylonitic deformation along GQVs. Feldspathisation and sericitisation are, in contrast, restricted to specific sectors and exposed as albitite, trondhjemite and pale green mica-rich outcrops. It is suggested that most of the exposed areas of the studied GQVs are, accordingly, not veins *sensu stricto* but metasomatic products where the original fabrics and features of precursor rocks were overprinted during coupled deformation and Si-metasomatism. Results presented here have major implications for the scale and geochemical behaviour of multi-metasomatic events, as well as on the kinetics of mineral replacement processes leading to changes in the physicochemical properties of crustal rocks.

Key words: giant quartz veins; granitoid; metasomatism; pyrenees; replacement veins

INTRODUCTION

Mineral replacement reactions are one of the underlying processes in the Earth's rock cycle. They are generally understood as the dissolution of a given mineral or group of minerals 'X_n' simultaneous to the precipitation of a new mineral or group of minerals 'Y_n' in the same place (Lindgren, 1925; Bastin *et al.*, 1931; Carmichael, 1987; Maliva & Siever, 1988; Fletcher & Merino, 2001; Wintsch & Yi, 2002; Putnis, 2009; Merino, 2017). Either coupled to volume changes (positive or negative; Weber *et al.*, 2021; Plümper *et al.*, 2022) or occurring at constant volume during replacement *sensu stricto* (Bastin *et al.*, 1931; Carmichael, 1987; Dewers & Ortoleva, 1989; Fletcher & Merino, 2001; Merino & Canals, 2011; Canals *et al.*, 2019), these mineral reactions are often invoked to drive compositional changes during rock metasomatism, i.e. a pervasive solid-state rock alteration through the introduction and/or removal of chemical components due to the interaction with aqueous fluids (Elburg *et al.*, 2001, 2012; Zharikov *et al.*, 2007; Engvik *et al.*, 2008; Harlov & Austrheim, 2012; Suikkanen & Rämö, 2019). Since the physicochemical properties of the replaced mineral/s (X_n) and the replacing mineral/s (Y_n) are normally different, replacement reactions involved in metasomatic processes result in significant changes of the rock properties. Therefore,

RECEIVED JULY 24, 2024; **REVISED** JANUARY 17, 2025; **ACCEPTED** JANUARY 21, 2025

replacement reactions and metasomatism have an influence on the rheological behaviour of the lithosphere (Wang et al., 2015; Wenker & Beaumont, 2018; Plümper et al., 2022) and on the concentration of rare earth elements, critical minerals and other types of ore deposits throughout the Earth's crust (Wilshire, 1984; Sillitoe, 2002, 2010; Seedorff et al., 2005; Cuney et al., 2012; Deymar et al., 2018; Groves et al., 2019; Gisbert et al., 2022). Furthermore, it has been suggested that some rocks of granitic appearance were not formed by igneous crystallisation: the granite-looking rocks at Mt. Painter Inlier (Northern Flinders Ranges, South Australia) were interpreted to have formed by the metasomatic alteration of the Radium Creek Group metasediments (Weisheit et al., 2013), and the Himalayan banded tourmaline leucogranites might have formed via metasomatism of a psammitic country rock (Dyck & Larson, 2023). These ideas refer back to the long-lasting magmatism *vs.* transformism debate on the origin of granites that took place from the late-19th to the mid-20th centuries, placing metasomatism back in the spotlight after more than half a century of paradigm-governed granite science where all granites are assumed to be magmatic in origin (Read, 1957; Clarke, 1996; González-Esvertit et al., 2025a).

Metasomatism can be driven by tectonic processes that operate at very different spatial and temporal scales, as well as by the availability and chemistry of circulating fluids and by the self-generated stress of metasomatic reactions (Putnis, 2009). The interplay between these boundary conditions may result in very different, often unusual, mineral assemblages. Accordingly, different types of metasomatism have been invoked for rocks with uncommon chemical compositions that cannot be named under the current classification schemes (Putnis & Austrheim, 2010). In this framework, prefixes based on the elements on which the studied rocks are enriched in, are common in the literature (among others, K-, Mg-, Na-, Ca-, Fe- and Si-metasomatism). In contrast, the coexistence or succession of different metasomatic reactions (i.e. multi-stage metasomatism), as well as the possible mineral transformations and their associated rheological and compositional changes, are difficult to assess due to the successive stages of textural and geochemical overprinting that rocks may experience.

The Variscan basement of the Pyrenees is a rich and diverse region in terms of metasomatised rock exposures (Schärer et al., 1999; Boulvais et al., 2007; Poujol et al., 2010; Fallourd et al., 2014; Boutin et al., 2016; Quesnel et al., 2019; Odlum & Stockli, 2020) (see a summary in Fig. 1). In fact, the Pyrenees can be considered as a region where uncommon rock types and mineralogical changes have historically been interpreted in very different ways. For example, this region turned out to be the flagship for the transformist ideas of the French school during the magmatism *vs.* transformism debate, being defined as a district in which remarkable rock transformations can be clearly seen (Lacroix, 1896, 1898; Adams, 1901; Guitard, 1953, 1955). Noteworthy, the term *episyenite* was coined in the Pyrenees to describe metasomatic syenites (Lacroix, 1920). Besides K-, Na-, Ca- and Mg-metasomatism already investigated in this region, the existence of a large number of quartz (Qtz) veins that are tens of metres wide and several kilometres long (i.e. Giant Quartz Veins; GQVs) has been reported (Autran & Guitard, 1968; Guitard, 1970; Ayora & Casas, 1983; Casas, 1984; Guitard et al., 1998a, 1998b; González-Esvertit et al., 2022a, 2022b). GQVs have been suggested to have formed, at least partially, through mineral replacement of the pre-existing host rocks during Si-metasomatism (González-Esvertit et al., 2022a, 2022b). These interpretations were based on qualitative observations made at the outcrop and thin section scale on GQVs hosted by metasedimentary rocks, which show relicts of precursor fabrics (bedding and foliation traces and ghost grains) and intense silicification aureoles in their adjacent host rocks (González-Esvertit et al., 2022a, 2022b). In the present work, we integrate qualitative observations with quantitative results to provide a multi-scale comparative appraisal of different metasomatic processes affecting granitoid rocks, as well as to assess their potential genetic relationship with the GQVs. Structural and petrographical characterisation, whole-rock geochemistry, Electron Backscatter Diffraction (EBSD) and database building are used to investigate pre-Variscan and late-Variscan unaltered granitoids and their corresponding alteration products, from the regional to the grain scale. The geochemical behaviour of three types of metasomatism (silicification, feldspathisation and sericitisation), their regional extent and the changes that they cause in the host-rock rheology are investigated. It is proposed that most of the exposed areas of the studied GQVs in the Canigó Massif are not veins *sensu stricto* but alteration products derived, at least partially, from the replacive silicification of the surrounding rocks. The studied processes yield new evidence for our understanding of petrogenetic processes involved in multi-stage metasomatism, shedding light on the kinetics governing mineral replacement reactions and providing new insights into heat and mass transfer and the fluctuations of rock physicochemical properties in the Earth's crust.

GEOLOGICAL BACKGROUND

The Pyrenees is an asymmetric, doubly verging, E–W trending Alpine fold-and-thrust belt that formed from the late Cretaceous to Miocene after the collision between the Iberian and Eurasian plates (Roest & Srivastava, 1991; Muñoz, 1992; Rosenbaum et al., 2002). Alpine deformation gave rise to an antiformal stack of pre-Alpine (Ediacaran to Carboniferous) basement rocks exhumed along the backbone of the cordillera (i.e. axial zone). The basement rocks of the Pyrenees lie geographically disconnected from other Palaeozoic outcrops of the Catalan Coastal Ranges, towards the south (Fig. 1), and the Mouthoumet and Montagne Noire massifs, towards the north, and are mainly composed of a metasedimentary succession that hosts Cadomian, Ordovician and Variscan magmatic rocks (Liesa et al., 2008, 2021; Casas et al., 2015, 2024; Navidad et al., 2018; Lemirre et al., 2019; Padel et al., 2022; Pujol-Solà et al., 2022). Basement rocks also record Sardic (Ordovician), Variscan and Alpine deformational events, as well as a high-temperature–low-pressure Variscan regional metamorphism (Guitard, 1970; Santanach, 1972a; Zwart, 1986; Casas, 2010; de Hoÿm de Marien et al., 2019; Muñoz, 2019; Puddu et al., 2019).

The most widespread igneous rocks in the Pyrenean basement are Variscan orthogneisses derived from late Neoproterozoic and Ordovician intrusives (Castiñeiras et al., 2008; Casas et al., 2010; Navidad et al., 2018) and late-Variscan granitoids (Autran & Guitard, 1957; Aguilar et al., 2014; Denèle et al., 2014; Lemirre et al., 2019; Liesa et al., 2021) (Fig. 1). Orthogneisses occur as domes surrounded by mid-to-high grade late Ediacaran-Ordovician metasediments. The Canigó Massif represents an E–W-trending antiformal macrostructure in the Eastern Pyrenees (Fig. 1), composed of ca. 3000 m-thick granitic orthogneisses with protoliths dated at ca. 457–464 Ma (SHRIMP U–Pb in zircon; Navidad et al., 2018). Guitard (1970) identified several gneiss types, namely the G1, G2 and G3 Canigó orthogneiss (Figs 2 and 3). Geochronological and geochemical data have demonstrated that they were formed in two different pulses during a 20 Ma period of Ordovician magmatic activity from the melting of a

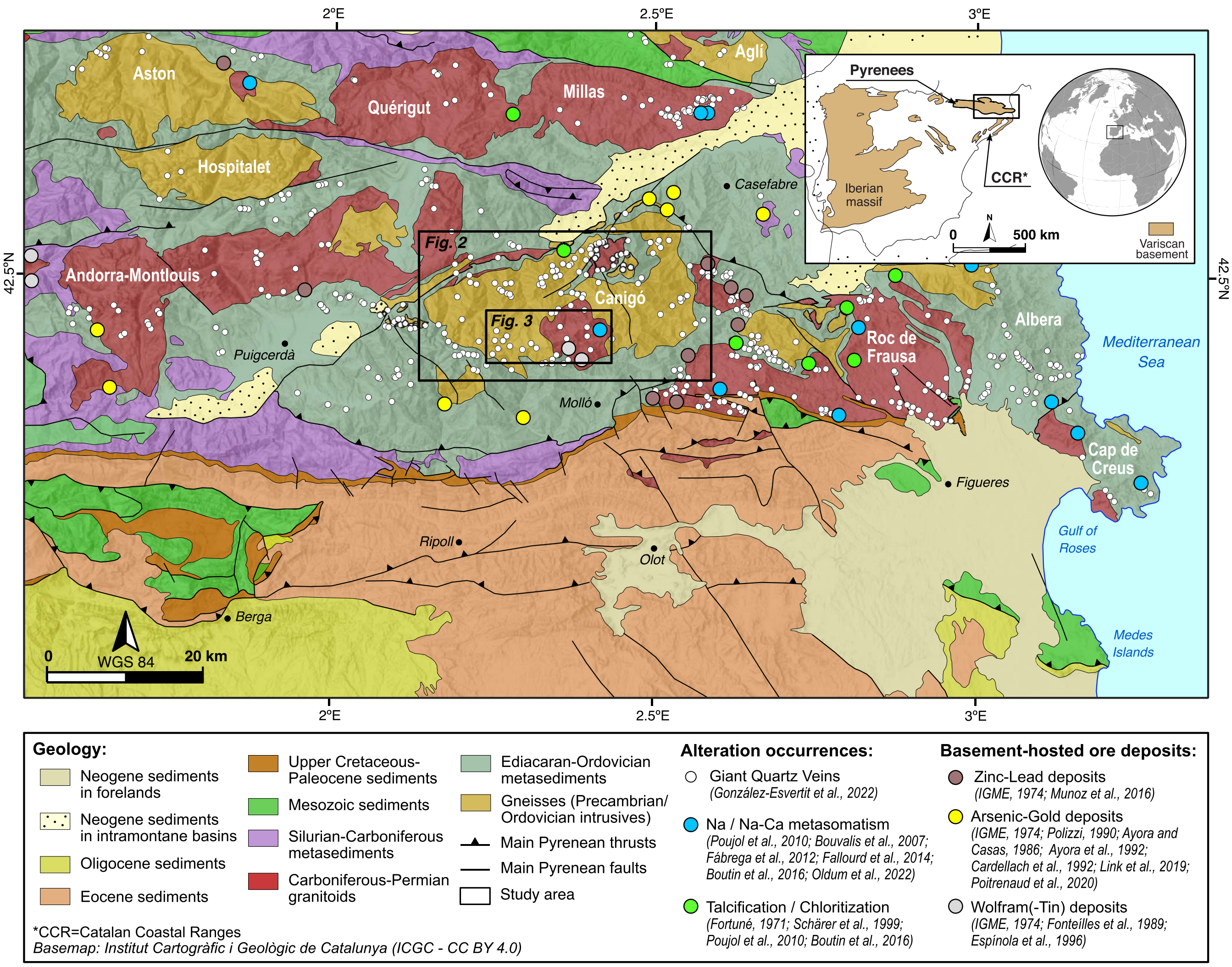

Fig. 1. Geological sketch map of the Eastern Pyrenees (SW Europe) with the main metasomatic rock occurrences (Fortuné, 1971; Schärer *et al.*, 1999; Boulvais *et al.*, 2007; Poujol *et al.*, 2010; Fàbrega *et al.*, 2012; Fallourd *et al.*, 2014; Boutin *et al.*, 2016; Odlum *et al.*, 2022; González-Esvertit *et al.*, 2022a) and ore deposits (IGME, 1972, 1974; Ayora & Casas, 1986; Polizzi, 1990; Ayora *et al.*, 1992; Cardellach *et al.*, 1992; Espinola *et al.*, 1996; Munoz *et al.*, 2016; Link *et al.*, 2020; Poitrenaud *et al.*, 2020) reported in the Variscan basement rocks. Base map: Hillshade Digital Elevation Model, Institut Cartogràfic i Geològic de Catalunya, ICGC.

heterogeneous late Neoproterozoic (Ediacaran) crust (Navidad *et al.*, 2018) (Fig. 2). The Canigó orthogneisses are intercalated in a ca. 4000-m-thick pre-Upper Ordovician metasedimentary sequence (Guitard, 1953; Laumonier, 1988; Padel *et al.*, 2018) (Figs 2 and 3). The part of this sequence underlying the Canigó gneisses corresponds to the Balaig Series (Guitard, 1953), composed of mid-to-high grade mica schists with marble, quartzite and metabasite intercalations. The most remarkable metaigneous intercalation in the Balaig Series is the Casemí orthogneiss (ca. 446–452 Ma, SHRIMP U–Pb in zircon; Casas *et al.*, 2010), a laccolithic body mainly made up of fine-grained granitic gneisses, up to 500-m-thick (Figs 2–4). The underlying Cadí granitic augen gneiss (ca. 456 Ma, SHRIMP U–Pb in zircon; Casas *et al.*, 2010), constitutes the deepest rocks of the massif. The Canigó orthogneisses separate the Balaig Series from the overlying Canaveilles and Jujols metasedimentary successions. The Canaveilles Group (former Canaveilles Serie of Cavet, 1957) is an Ediacaran-Terreneuvian heterolytic unfossiliferous succession, up to 1500-m-thick, mainly composed of metapelites interbedded with quartzites, marbles, calc-silicate rocks, felsic metatuffs and metabasites. The Jujols Group is a monotonous succession of metasiltstones with a depositional age bracketed between the Terreneuvian and the Furongian–Early Ordovician (Fig. 2) (Padel *et al.*, 2018). The whole metasedimentary sequence is unconformably overlain by the Upper Ordovician succession (Hartevelt, 1970; Santanach, 1972a) (Fig. 2). In the central area of the Canigó Massif, the late-Variscan Costabona granitoid crops out (Figs 1–3) and consists of a peraluminous biotite-bearing monzogranite with K-feldspar (Kfs) megacrysts. The Costabona granitoid has been dated at 285.4 ± 2.2 Ma and 302 ± 4 Ma (LA-ICPMS in zircon; Laumonier *et al.*, 2015), thus postdating the polyphase Variscan deformation (late Visean to Serpukhovian; Martín-Closas *et al.*, 2018), as well as the Variscan regional metamorphism (Autran *et al.*, 1970; Guitard, 1970; Casas, 1984; Zwart, 1986) (Fig. 2).

The study area is located in the southern part of the Canigó Massif (Figs 2–4). In its western sector, the G1 and G2 Canigó orthogneisses are the most abundant rock types (Fig. 4B), whereas eastwards, the Canaveilles micaschists, the G1 and G2 Canigó orthogneisses and the Costabona monzogranite extensively crop out (Fig. 4A and C). The field, textural and mineralogical, and geochemical characteristics of unaltered and altered rock units of the study area are provided below.

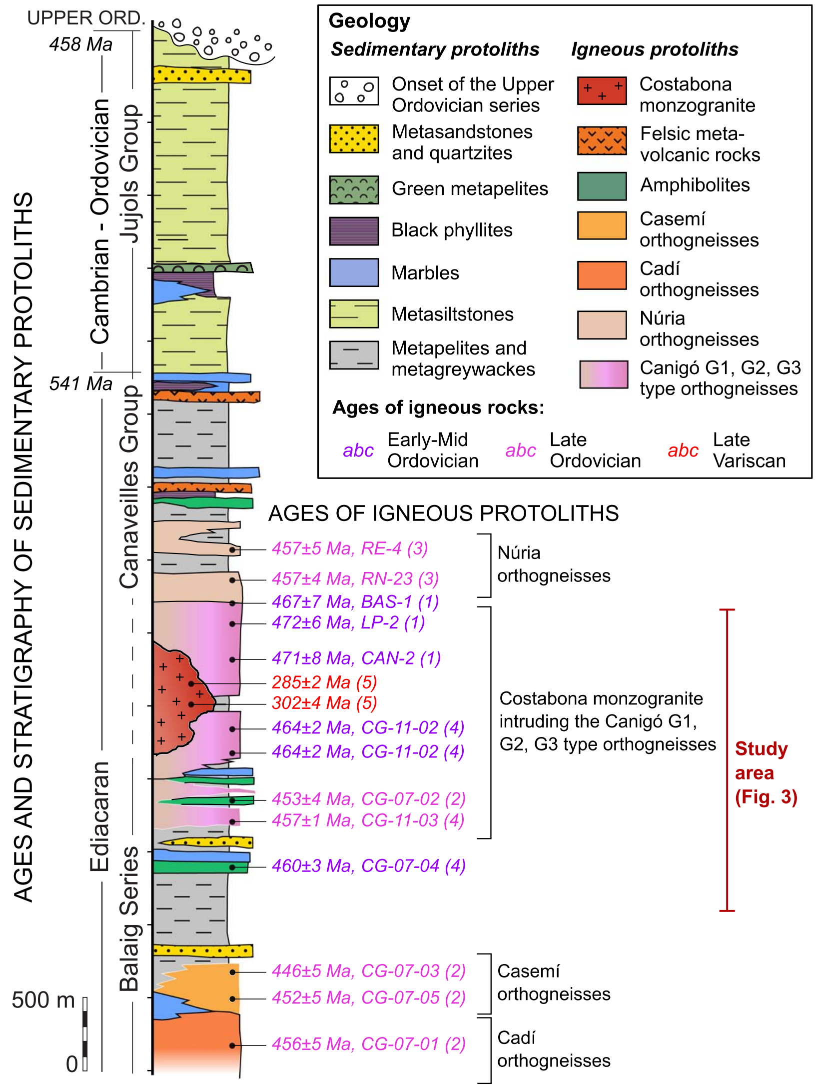

Fig. 2. Synthetic stratigraphic column of the rocks cropping out in the Canigó Massif (adapted from Casas *et al.*, 2019 after compilations from Castiñeiras *et al.*, 2008; Casas *et al.*, 2010; Navidad *et al.*, 2010, 2018; Martínez *et al.*, 2011). Stratigraphic data from Guitard (1970), Santanach (1972b), Ayora & Casas (1986) and Liesa & Carreras (1989); geochronological data from (1) Cocherie *et al.* (2005), (2) Casas *et al.* (2010), (3) Martínez *et al.* (2011), (4) Navidad *et al.* (2018) and (5) Laumonier *et al.* (2015).

METHODS

Descriptive approaches, analytical methods and comparative procedures have been employed in the present work to obtain a multi-scale assessment of the investigated metasomatic processes. Groundwork was based on field investigations for the mapping, structural analysis and sampling of the unaltered rocks, their alteration products and their associated deformation mesostructures. Bulk-rock geochemical composition of selected samples was then determined and combined with the mining, curation and harmonisation process of all the available whole-rock geochemical data of granitoid rocks in NE Iberia (the North-East Iberian GRAnitoids, NEIGRA database; González-Esvertit *et al.*, 2024b). Mass-balance modelling between unaltered and altered rocks was also carried out to evaluate elemental gains and losses occurred during metasomatism. Investigations at the cm- to μm-scale were based on spatially resolved cm-scale bulk-rock analyses, mineral phase abundance quantification trough image segmentation and crystal orientation determination for the identification of mineral replacement behavio ur and deformation mechanisms. Further details on database building, geological mapping, sample rationale, whole-rock geochemistry, EBSD and mass-balance modelling are provided in the Supplementary Material 1 (SM1).

RESULTS

Field relationships and rock microstructures

Unaltered rock units

Metasedimentary rocks in the study area correspond to the fine-grained, low- to mid-grade biotite- and muscovite-rich metapelites and metagreywackes of the Canaveilles Group (Fig. 5A and E). They contain minor cordierite and andalusite porphyroblasts, and occasional tourmaline, zircon, apatite and ilmenite accessory minerals. A dominant NE–SW-trending foliation is the most recognisable meso- and microstructure in the metasediments. This foliation is defined by the orientation of biotite and muscovite crystals and a compositional banding formed by 1–4 cm-thick Qtz- and mica-rich layers. An E–W-trending N-dipping crenulation cleavage occurring at high angle to the dominant foliation surfaces,

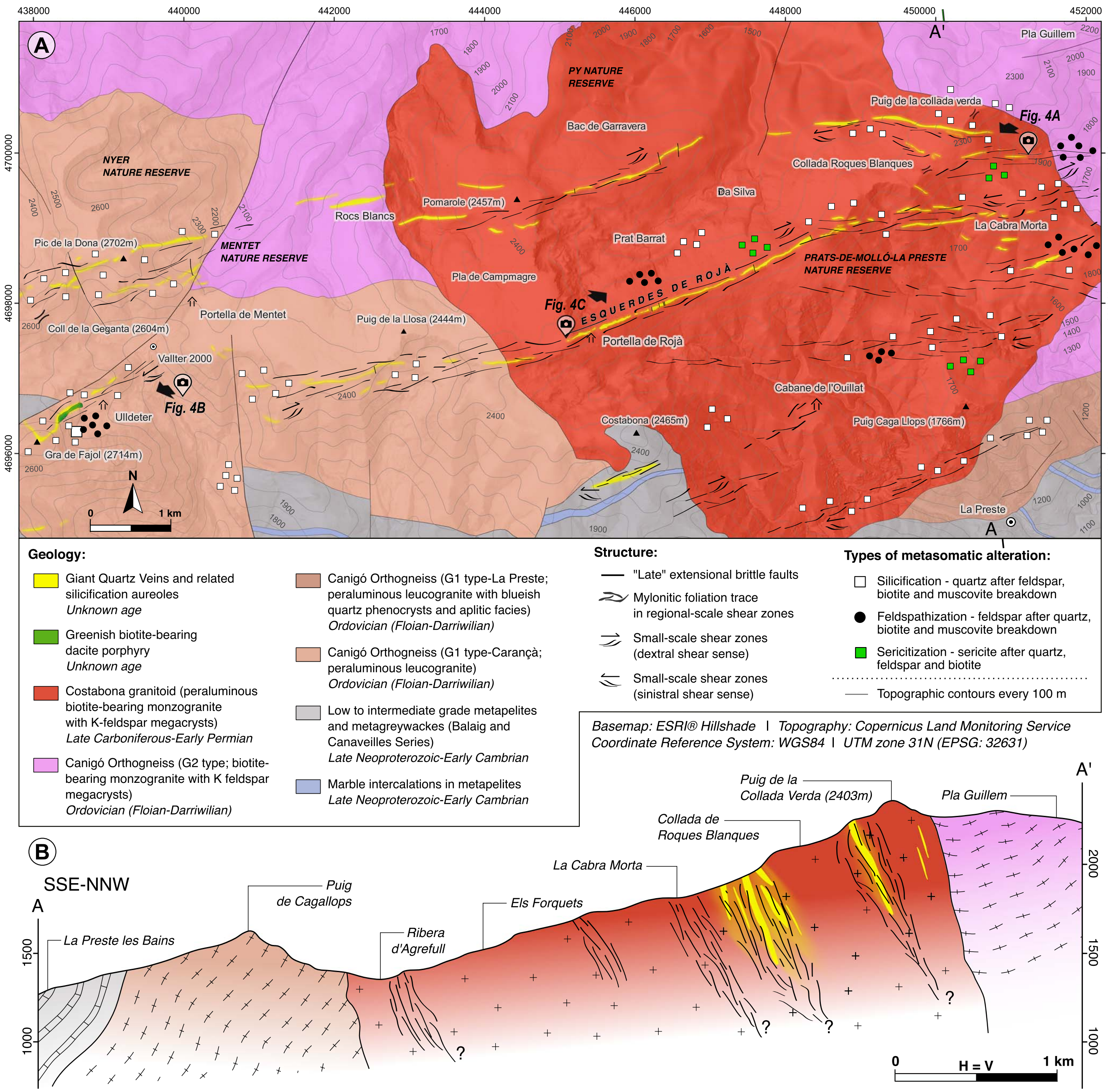

Fig. 3. (A) Geological-structural map of the southern part of the Canigó Massif with the location of different types of alteration affecting the Canigó gneiss and the Costabona monzogranite. Location of panoramic views in Fig. 4 are indicated. (B) SSW–NNE schematic cross section representative of the study area, modified after Casas (1984). Base map: Hillshade (ESRI®) and Topography from Copernicus Land Monitoring Service.

and associated with folds, is also recognisable (Fig. 5A). At the microscopic scale, lepidoblastic muscovite layers with kink-type folds (Fig. 5E), as well as recrystalised textures dominated by grain boundary migration in Qtz-rich domains, are the most noteworthy microstructures (see more details in Fig. S1; Supplementary Material 1).

The Canigó orthogneisses extensively crop out in the study area (Figs 2 and 3). Three orthogneiss types have been differentiated within this unit on the basis of their mineralogy and microstructure (Guitard, 1965, 1970). The Canigó G1 type-La Preste crops out in the southeastern sector of the study area, consisting of a ca. 1000-m-thick light-coloured biotite-poor orthogneiss body with Kfs (1–5 cm in size) and blueish Qtz (0.5–2 cm in size) porphyroclasts. This unit shows a massive aspect and a poorly developed NE–SW-trending and SE-dipping gneissic foliation. The Canigó G1 type-Carançà Orthogneiss is present along the southwestern sector of the study area (Fig. 3) and is characterised by the absence of blueish Qtz porphyroclasts and a higher biotite and Kfs porphyroclast content respect to the Canigó G1 type-La Preste. The gneissic foliation and lineation are well developed and show the same structural attitude in both orthogneiss units (Fig. S1; Supplementary Material 1). The Canigó G2 Orthogneiss (Fig. 5B, E and F) extensively crops out along the northwestern and northeastern sectors of the study area (Figs 2 and 3), structurally below the G1 orthogneisses (Casas, 1984). The G2 orthogneisses are coarse-grained, biotite-rich with very well-developed gneissic

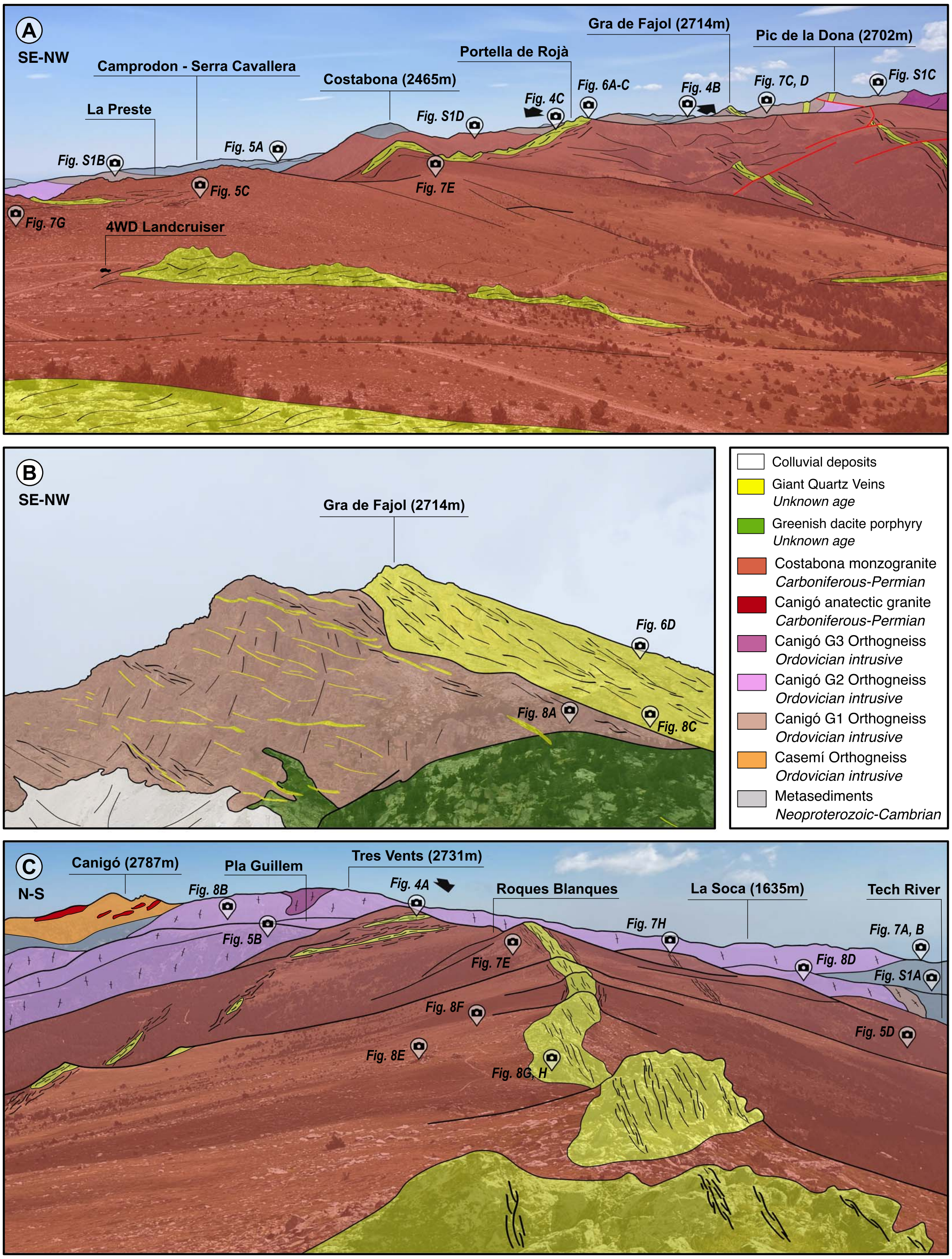

Fig. 4. Panoramic views of three representative sectors of the study area. (A) From the Collada de Roques Blanques area to the Pic de la Dona summit (view towards SW). (B) From the Ulldeter area to the Gra de Fajol summit (view towards SW). (C) From the Portella de Rojà to the Canigó summit (view towards NNE). See Figs 2 and 3 for locations and Supplementary Material 1 (Fig. S2) for uninterpreted versions of the photographs.

foliation and lineation, have a relatively homogeneous composition (Fig. 5B), and often exhibit Qtz and Kfs porphyroclasts with rapakivi textures. At the thin section scale, Qtz (0.2–0.8 cm in size) and feldspar (0.5–2 cm in size) σ-type mantled porphyroclasts are embedded within a strongly foliated Qtz-feldspar matrix rich in biotite and muscovite (Fig. 5F). In Qtz-rich matrix domains there is evidence of dynamic recrystallisation by means of grain boundary migration with associated pinning and dragging microstructures (Jessell, 1987; Passchier & Trouw, 1996). Orthoclase and microcline crystals often show perthitic exsolution, forming a light-coloured irregular lamellae, as well as Carlsbad and cross-hatched tartan twinning patterns, respectively. Occasionally, the G2 type Orthogneiss shows 0.5–8-m-thick intercalations of fine-grained, biotite-poor leucocratic gneiss bands.

The Costabona monzogranite (Fig. 5C, E and G) crops out in the central and eastern sectors of the study area (Figs 3 and 4A, C) and is characterised by microcline and orthoclase phenocrysts (1–8 cm in size) embedded in a quartzofeldspathic xenomorphic matrix rich in biotite and, occasionally, oligoclase and muscovite. At the outcrop scale, 6–40 cm long tonalite enclaves (Fig. S1;

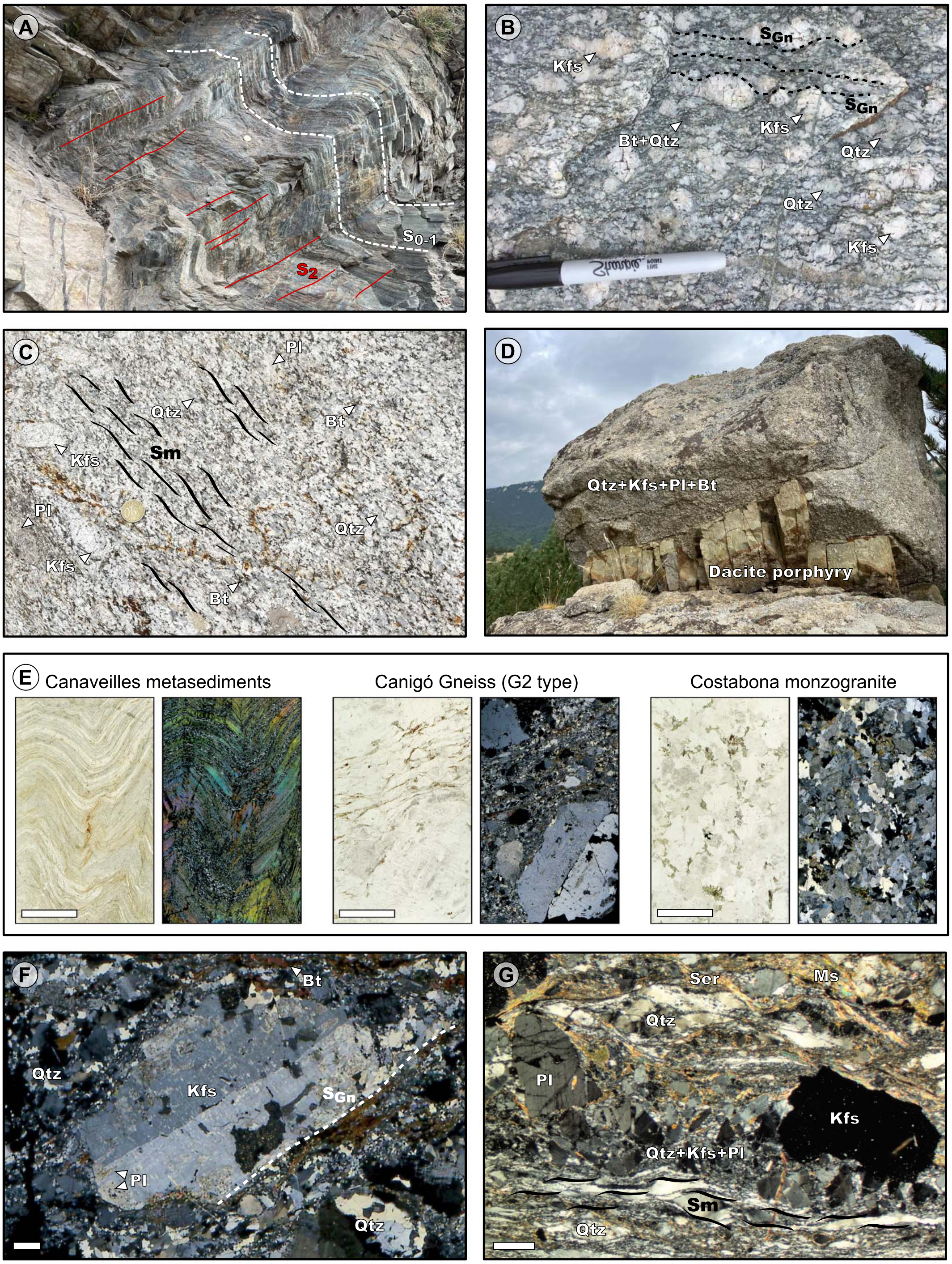

Fig. 5. Representative outcrop (A-D) and microstructural (E-G) features of the unaltered rock units in the study area. (A) Canaveilles micaschists exhibiting a dominant cleavage (S_{0-1}) and a crenulation cleavage (S_2) parallel to mesoscale folds. (B) Canigó G2 orthogneiss showing a massive character with Qtz and Kfs porphyroclasts embedded in a biotite (Bt)-rich matrix with a well-defined gneissic foliation (S_{Gn}). (C) Costabona monzogranite exhibiting Kfs and plagioclase (Pl) phenocrysts; note the presence of a mylonitic foliation (Sm) defined by the orientation of mica crystals. (D) Dacite porphyry dyke (0.4-m-thick) crosscutting the Costabona monzogranite. (E) Representative thin sections of the Canaveilles micaschists, the Canigó G2 Orthogneiss and the Costabona monzogranite in plane polarised light (PPL; left) and crossed polars (XPL, right). (F) Kfs σ-type porphyroclast from the Canigó G2 orthogneiss; note incipient sericitisation and perthitic unmixing in Kfs. (G) Deformed Costabona monzogranite affected by the Sm, showing dynamically recrystallised Qtz and fractured feldspar porphyroclasts. See Figs 2–4 for locations and Supplementary Material 1 (Fig. S1) for more details. Scalebars are 1 cm for panel E and 0.25 mm for panels F and G. Mineral abbreviations following Warr (2021).

Supplementary Material 1), as well as microcline phenocrysts with biotite inclusions and Carlsbad twinning patterns, are characteristic features.

The Costabona monzogranite and the Canigó orthogneisses are deformed by an ENE–WSW-trending and NNW-dipping mylonitic foliation that is also recorded in the GQVs (see description below) (Fig. 5C and G) (Casas, 1984, 1986). Within mylonitic bands, foliation is well defined by the orientation of muscovite and biotite crystals forming S-C fabrics, Qtz ribbons, elongation of monocrystalline Qtz porphyroclasts and by Qtz dynamic recrystallisation.

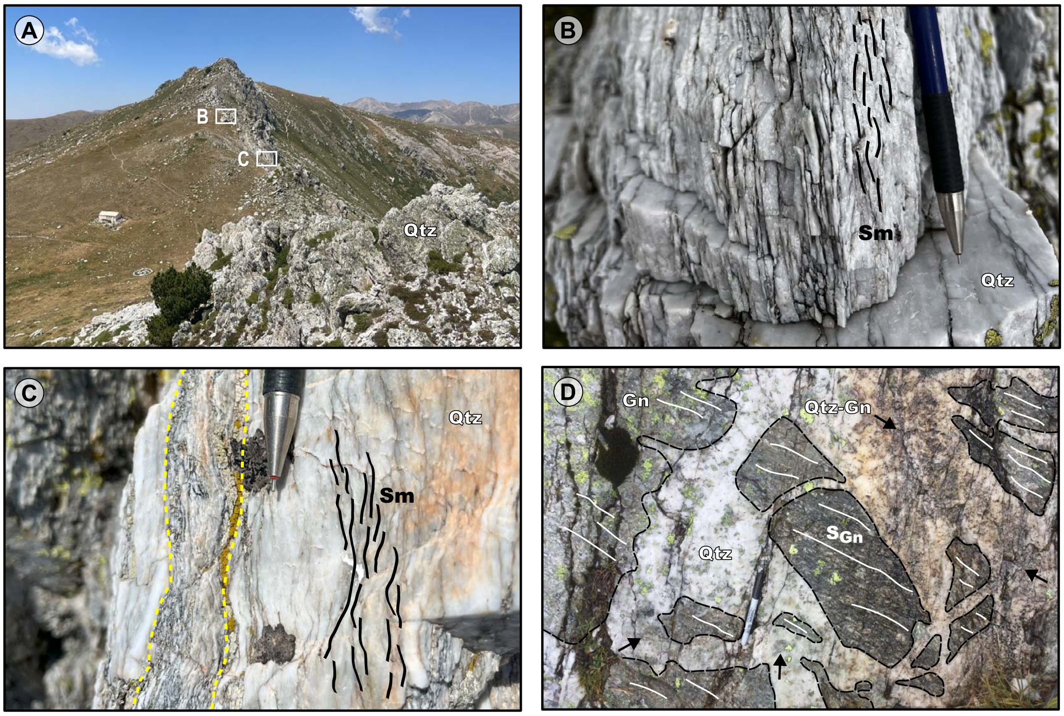

Fig. 6. Representative outcrop photographs of the GQVs of the Canigó Massif. (A) The Esquerdes de Rojà GQV, inferring a positive topographic relief of more than 100 m with respect to the surrounding areas (mountain shelter at the left side of the vein for scale). (B) ENE–WSW-trending mylonitic bands defining a continuous foliation (Sm) in the central area of a GQV. (C) Cataclastic grain-size reduction bands (yellow) occurring parallel to the Sm in the central area of a GQV. (D) Orthogneiss fragments within a GQV; note that the orientation of the gneissic foliation (S_{Gn}) is constant in the different, isolated blocks; black arrows indicate transitional zones between GQV Qtz and gneiss (Qtz-Gn). See Figs 3 and 4 for locations and Supplementary Material 1 (Fig. S3) for microstructure details. Mineral abbreviations following Warr (2021).

Partial silicification is often spatially related to these mylonitic bands, and the macro- and microstructural fabrics are similar for the Costabona granite and the Canigó orthogneisses. Mylonites contain Qtz and microcline crystals acting as Φ- and σ-type porphyroclasts (Fig. 5G), as well as fish-shaped muscovite crystals (Fig. S1; Supplementary Material 1).

Several 0.2–1.5-m-thick dykes of greenish, biotite-bearing dacite porphyry are also present in the study area and crosscut both the Canigó orthogneisses and the Costabona monzogranite (Fig. 5D). They postdate the development of the gneissic foliation in the Canigó orthogneisses, as well as the emplacement of the Costabona monzogranite. The largest exposure has been identified at the base of the Gra de Fajol summit (Fig. 3) and corresponds to a ca. 25-m-thick dyke, which crosscuts the Canigó G1 type-Carançà Orthogneiss and is crosscut by the Gra de Fajol GQV (Fig. 4B).

A significant number of GQVs cross-cut the Canaveilles micaschists, the Canigó orthogneisses, the Costabona monzogranite and the greenish dacite porphyry dykes (Figs 3, 4 and 6). These GQVs generally occur as discontinuous Qtz bodies that are tens of meters wide and hundreds to thousands of meters long (up to 11 km for the Esquerdes de Rojà GQV; Fig. 3). The cores of the GQVs (Fig. 6B and C) are entirely composed of Qtz with sporadic occurrence of fuchsite, a greenish, chromium-rich variety of muscovite. The boundaries of these Qtz accumulations (Figs 6D and 8E–H) are diffuse and record a progressive silicification that is exceptionally well exposed as symmetric alteration haloes affecting the host rocks. About 10% of the volume of the GQVs is also formed by accumulations of crack-seal small-scale Qtz veins with complex crosscutting relationships. Vein Qtz and silicified host rocks often record the ENE–WSW-trending mylonitic foliation that also affects the Costabona monzogranite and the Canigó orthogneisses (Fig. 3). The development of mylonitic foliation varies between different vein Qtz outcrops and, sometimes, even within the same outcrop. Mylonitic foliation shows low-strain domains with at most incipient development and high-strain domains with complete Qtz recrystallisation (Fig. 6B and C). Cataclastic bands (1 to 8 cm-thick) that show grain-size reduction processes are also present (Fig. 6C). A subvertical N-S-oriented brittle fracture system postdates both the mylonitic foliation and the cataclastic bands.

At the thin section scale, GQV Qtz shows a wide range of deformation microstructures (see detailed summary and microphotographs in Fig. S3; Supplementary Material 1). Protocataclastic to cataclastic bands, where there is no Crystallographic Preferred Orientation (CPO), show microstructures indicative of pressure-solution, such as aligned grain boundaries and solution seams. Crystal-plastic deformation is present as protomylonite to ultramylonite areas with S-C fabrics and, in some cases, C′ shear bands, where Qtz is dynamically recrystallised through bulging and sub-grain rotation recrystallisation (Hirth & Tullis, 1992; Stipp *et al.*, 2002).

Metasomatic products

Metasomatic alteration of the Canaveilles micaschists, Canigó orthogneisses and Costabona monzogranite is well exposed throughout the study area (Figs 7–9). In the Canaveilles micaschists, gradual transitions from the metasediments towards a quartzofeldspathic rock with a chiefly polygonal fabric are noteworthy. These transitions are represented by a gradual disappearance of micas and foliation surfaces, as well as by

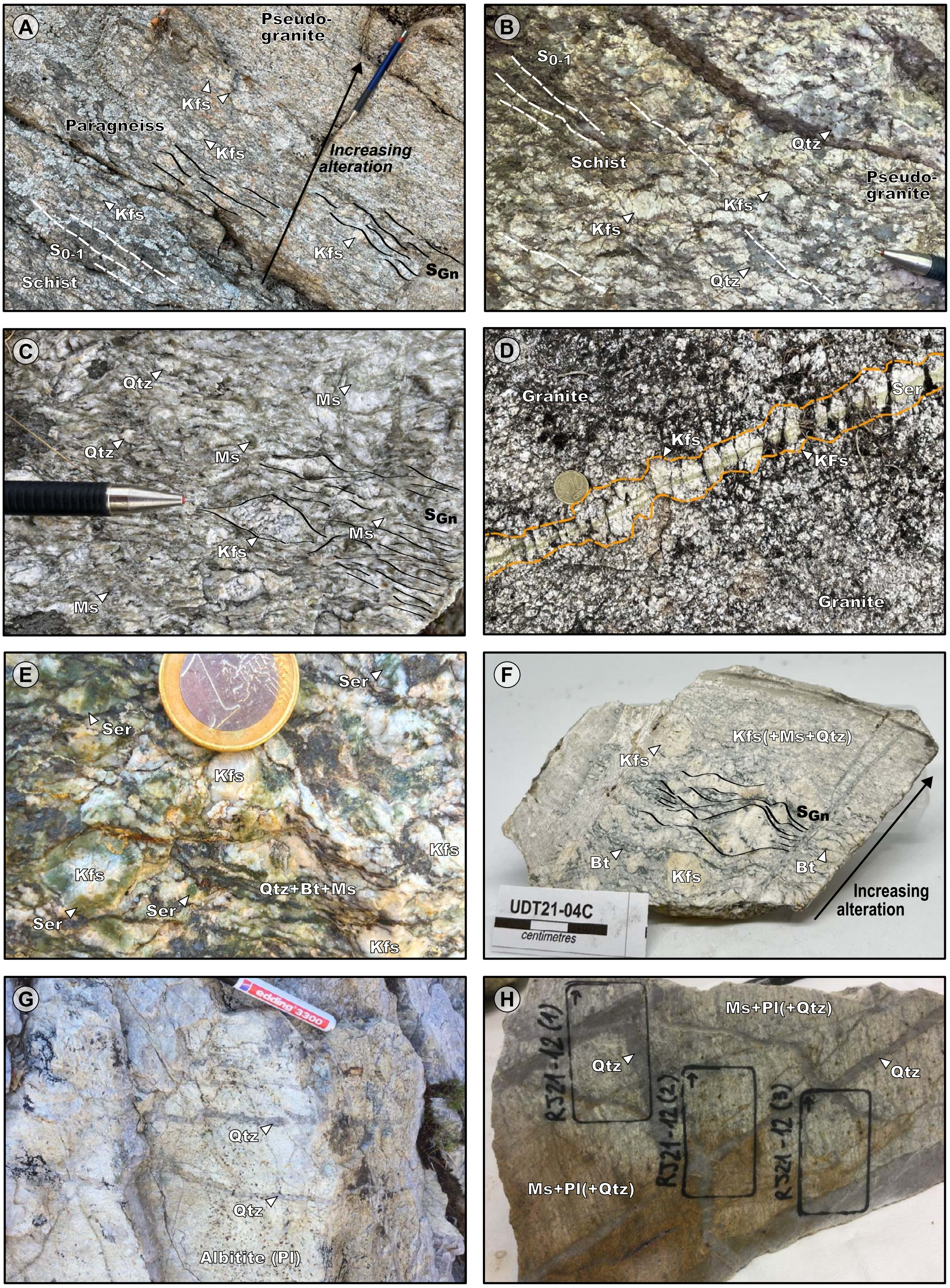

Fig. 7. Representative features of the metasomatic alterations exposed in the Canigó Massif. (A and B) Gradual transitions from micaschists to a quartzofeldspathic rock, 'pseudo-granite', where remnants of the dominant cleavage (S_{0-1}) are present; note the progressive gain Kfs porphyroblasts with increasing alteration. (C–E) Sericitisation processes along (C) the gneissic foliation (S_{Gn}), (D) a Kfs vein and (E) Kfs porphyroclast grain boundaries. (F–H) Feldspathisation processes affecting the Canigó orthogneiss (F; Kfs episyenite) and the Costabona monzogranite (G and H; Pl-feldspar episyenite); note that the alteration in (F) produces a decrease in the rock Bt content, resulting in a mineral assemblage composed of Kfs with minor Qtz and muscovite (Ms). See Figs 3 and 4 for locations. Mineral abbreviations following Warr (2021).

variations in crystal size (Fig. 7A and B). They often occur in single outcrops (transition lengths between 10 cm and 5 m), and the alteration end-member resembles a granite in terms of texture and mineral assemblage. We therefore use the term 'pseudo-granite' for this altered rock. The dominant cleavage surfaces of the precursor micaschists are sometimes recognisable within the pseudo-granites and show a similar structural attitude as in the rest of the study area. Occasionally, a transitional rock with authigenic Kfs megacrysts (i.e. porphyroblasts) and a well-developed gneissic foliation parallel to the dominant cleavage surfaces is present between the micaschist and pseudo-granite end-members (Fig. 7A). In other cases, the transition occurs in

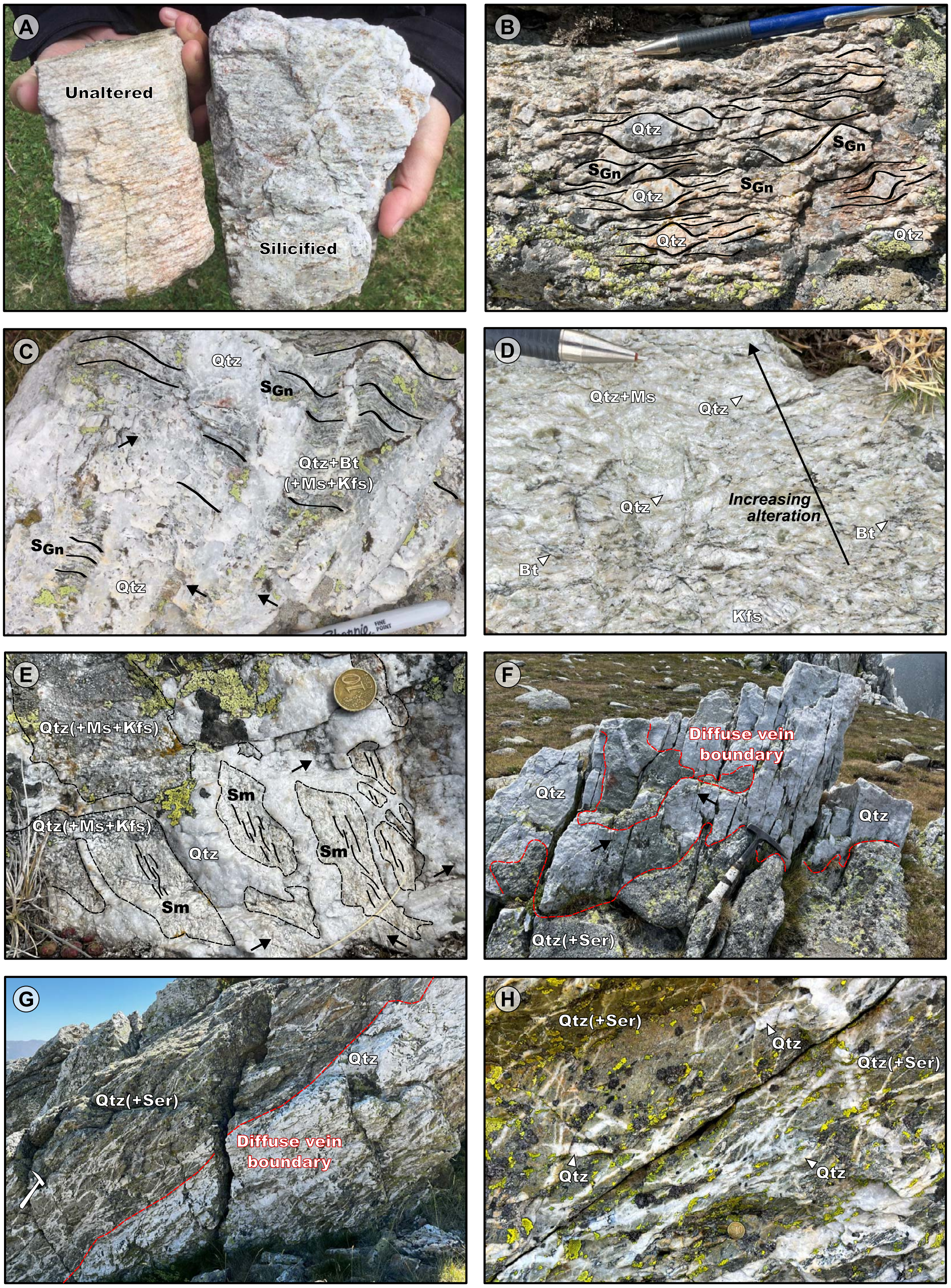

Fig. 8. Representative features of the silicification processes exposed in the Canigó Massif. (A) Colour variations caused by mineralogical changes during orthogneiss silicification. (B) Silicified orthogneiss outcrop showing Qtz pseudomorphs after Kfs porphyroclasts. (C) Isolated fragments of silicified orthogneiss at GQV boundaries; note that the trend of the S_{Gn} surfaces is similar in all isolated fragments, and that there are transition zones where remnants of the orthogneiss fabrics are present within the GQV Qtz. (D) Silicification, sericitisation and Bt breakdown affecting orthogneisses. (E) Fragments of granite mylonite along a GQV boundary; note that the GQV Qtz is not affected by the mylonitic foliation (Sm) that is recorded in the host-rock fragments. (F) Diffuse GQV boundary where transitional areas between the altered host rocks and GQV Qtz are exposed (black arrows). (G) Diffuse vein boundary with Qtz vein networks; note that host-rock fabrics are preserved within the GQV Qtz. (H) Pale-green host rock composed of Qtz and sericite (Ser) being crosscut by cm-wide veins (detail of G). See Figs 3 and 4 for locations. Mineral abbreviations following Warr (2021).

a more restricted space and only a few centimetres separate the schists from the pseudo-granitic rock, where the latter still records ghost traces of the dominant cleavage surfaces (Fig. 7B). Nevertheless, due to the presence of other granitic rocks in the study area and their intricate structural relationships, it has not been possible to determine the regional extent of this solid-state rock transformation.

Sericitisation (i.e., sericite and minor muscovite gain, Qtz, biotite and feldspar breakdown; Figs 7 and 9), feldspathisation (i.e. episyenitisation; feldspar gain, Qtz and mica breakdown;

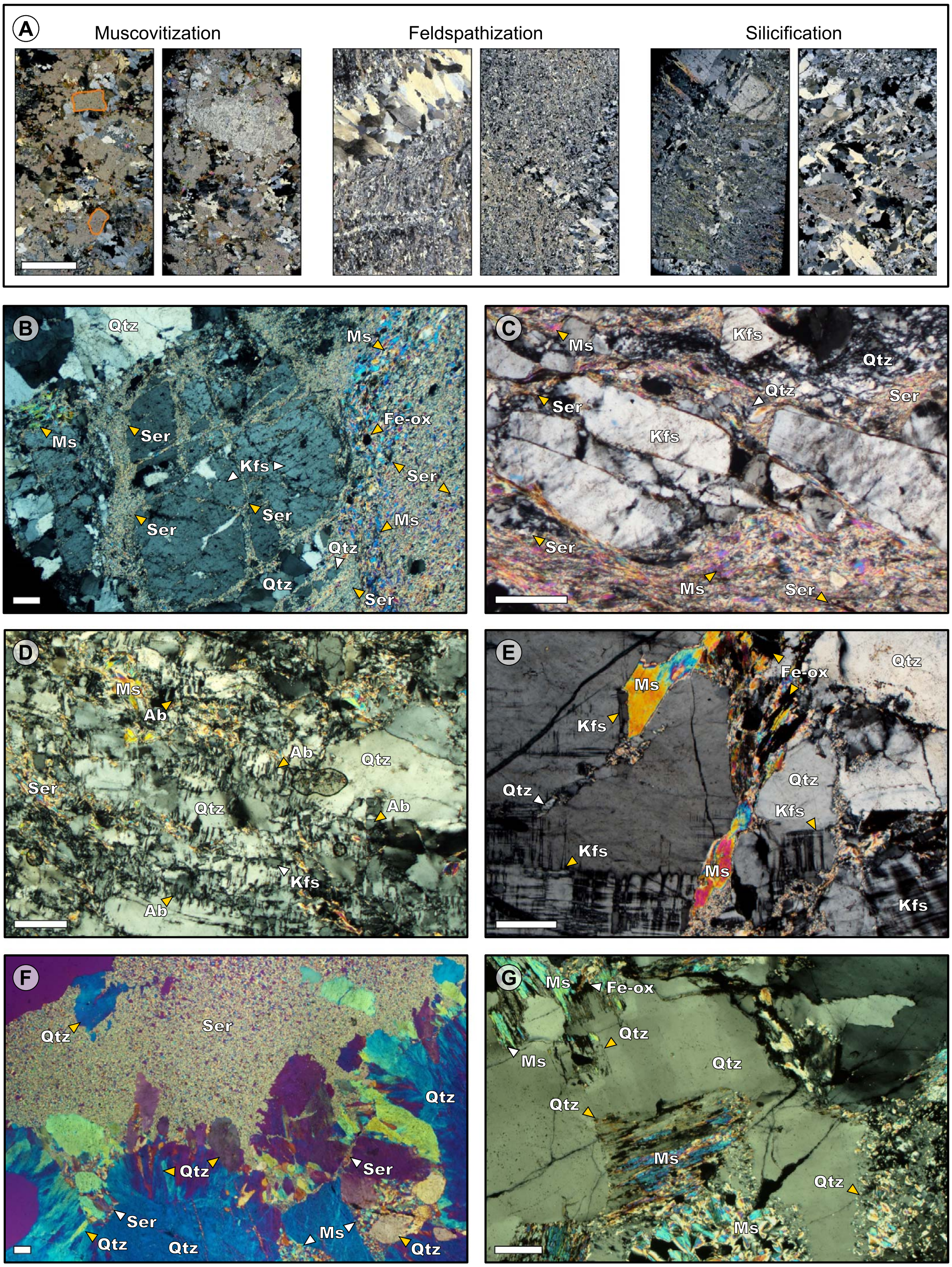

Fig. 9. Summary of the petrographic features of the altered rock units in the study area; orange arrows indicate the replacing mineral, white arrows indicate replaced minerals. (A) Representative thin sections of the sericitisation, feldspathisation and silicification alteration types exposed in the study area (XPL); orange outlines in the left image indicate Kfs pseudomorphs formed by white mica aggregates. (B and C) Sericitisation (Ser) and muscovitisation (Ms) affecting Qtz and Kfs crystals following (B) brittle fractures and (C) the gneissic foliation (S_{Gn}). (D and E) Feldspathisation affecting the Costabona monzogranite by means of (D) albitisation (Ab) and (E) microclinisation (Kfs) of Qtz and Ms; note that newly formed albite and microcline show characteristic chessboard and cross-hatched tartan twinning patterns. (F and G) Silicification processes affecting the Costabona monzogranite; in (F), Qtz overgrows a previously sericitised area; in (G), Ms and Ser pseudomorphs are replaced by Qtz, leaving ghost traces of the original shapes and exfoliation surfaces of crystals. Scalebars are 1 cm for panel A and 0.25 mm for panels B-G. Mineral abbreviations following Warr (2021).

Figs 7 and 9) and silicification (i.e., Qtz gain, feldspar and mica breakdown; Figs 8 and 9) are the most common alteration styles in the study area and are generally recorded in the Canigó orthogneisses and the Costabona monzogranite. Sericitisation, which is sometimes spatially related to GQVs and mylonite bands (Fig. 3), is generally restricted to the easternmost sector of the study area affecting the Costabona monzogranite (Fig. 7D and E) and, more rarely, the Canigó orthogneisses (Fig. 7C). At the outcrop scale, rocks exhibiting this alteration are characterised by the partial or complete replacement of Kfs, biotite and Qtz by muscovite and sericite, giving rise to very characteristic pale green mica-rich outcrops (Fig. 7C–E). Rock fabrics and microstructures appear to have controlled, at least partially, the spatial distribution of this alteration, as demonstrated by vein-shaped (Fig. 7D) and foliation-parallel (Fig. 7C) sericitised areas. Altered outcrops show muscovite and sericite pseudomorphs of partially to completely replaced Kfs crystals, suggesting that this replacement has most likely occurred at an approximately constant volume (Fig. 7E). At the thin section scale, sericitisation is characterised by sericite and minor muscovite replacing Kfs and Qtz following pre-existing microstructures such as brittle fractures (Fig. 9B) or foliation surfaces (Fig. 9C). Fe-oxides are also present as an accessory phase in sericitised samples (Fig. 9B). Biotite is absent both at the outcrop and thin section scales. In some samples, sericite and muscovite have entirely replaced the Kfs megacrysts and they appear as large (0.5–1.5 cm in size) pseudomorphic aggregates of white mica (Fig. 9A).

Feldspathisation processes are widespread throughout the study area, forming leucocratic microclinite (Figs 7F and 9E) and albitite (Figs 7G, H and 9D) outcrops that in some cases are spatially related to GQVs and shear zones (Fig. 3). Relicts of the original rock fabrics and microstructures can be identified in moderately feldspathised areas, such as the gneissic and mylonitic foliation surfaces, respectively, in the Canigó G1 Orthogneiss (Fig. 7F) and the granite-mylonites derived from the Costabona monzogranite (Fig. 7H). Completely altered rocks, however, show a massive character with polygonal textures, without either muscovite or biotite (Fig. 7G). As for the sericitisation areas, episyenitisation is not always spatially related to GQVs (Fig. 3). However, cm-scale Qtz veins with blocky or elongated-blocky textures are common in the albitised areas (Fig. 7G and H). At the thin section scale, albitised rocks show unusual chessboard-twinned albite crystals replacing Qtz and Kfs, as well as minor muscovite (Fig. 9D). Minor relicts of non-replaced Kfs, as well as sericite clusters that could have replaced Kfs crystals and are currently replaced by albite, are also present. K-feldspathisation is, in contrast, characterised by replacement textures of muscovite and Qtz by microcline with distinctive cross-hatched tartan twinning. Relicts of the replaced minerals are well exposed as pseudomorphs or isolated remnants, which are more abundant close to the microcline replacement front yet also present within microcline crystals (Fig. 9E). Fe-oxides are also present in some sectors affected by feldspathisation (Fig. 9E).

Silicification (Figs 8 and 9F, G) is the most widespread alteration style in the study area and appears in all cases to be spatially related to GQVs and mylonitic bands, such as the Esquerdes de Rojà GQV and the La Cabra Morta mylonitic band (Figs 3 and 4). It often forms symmetric alteration haloes following the structural trend of GQVs, imparting significant colour changes to the pre-existing rock units, clearly recognisable in the Canigó orthogneisses (Fig. 8A–C) and the Costabona monzogranite (Fig. 8D–F). The intensity of silicification shows a gradual change with decreasing distance towards the GQVs. At tens to hundreds of meters away from the GQV to which it is associated, host-rock silicification is partial and the original fabrics of the precursor rocks are clearly recognisable (Fig. 8A and B). In these cases, biotite breakdown (Fig. 8A and D) and feldspar porphyroclast pseudomorphs formed by Qtz (Fig. 8B) are the most diagnostic features. Occasionally, progressive biotite breakdown can be identified at the cm-scale and is also associated with an increase of muscovite content (Fig. 8D).

As the distance to the GQVs decreases, silicification becomes more intense. Here, silicified host rocks often occur as rounded to subangular fragments of variable size that are embedded in a Qtz matrix formed by irregularly-shaped patches (Figs 6D and 8C, E, F). The shape of the host-rock fragments is highly variable, and they do not show a preferred elongation direction. Between the Qtz patches and the highly silicified host-rock fragments, transitional areas are common and exhibit ghost traces of the precursor structural features (see black arrows in Figs 6D, and 8C, E, F). The host-rock fragments, Qtz matrix and transitional areas define a replacement texture at the outcrop scale that gives rise to extremely diffuse and irregular vein boundaries (Fig. 8F–H). Relict grains, foliations and lineations present in the silicified host rocks often show a continuity towards the inner parts of the GQVs (Fig. 6D), where ghost minerals and pseudomorphs are also common. Noteworthy, planar mesostructures within silicified host-rock fragments forming the GQV boundaries show the same structural trend when comparing different fragments in the same outcrop or even different fragments from different outcrops (Figs 6D and 8C, E). This phenomenon is well recognisable for the gneissic foliation surfaces within these fragments, whose orientation (*strike/dip*: 062/58; average pole to plane: 332/32) is equal to the regional structural trend measured throughout the study area (*strike/dip* of 061/47; average pole to plane of 331/43) (Fig. 10A). Occasionally, the diffuse vein boundaries also show a complex network of cm-wide Qtz veins crosscutting a highly silicified pale-green host rock entirely composed of Qtz and sericite (Fig. 8G and H).

At the thin section scale, silicification sectors show an increasing proportion of xenomorphic to subidiomorphic Qtz crystals (Fig. 9F and G). Qtz replaces Kfs megacrysts (Fig. 9A), sericite masses (Fig. 9F) and euhedral muscovite crystals (Fig. 9G) following replacement fronts or vein-shaped structures. Isolated remnants of the replaced minerals within the replacing Qtz (Fig. 9F), as well as mineral pseudomorphs and ghost grains (Fig. 9G), are the most common microstructures indicating replacement. The replacement of feldspar by Qtz occurs as a two-step reaction by which sericite and muscovite replace feldspar and are subsequently replaced by Qtz. Accordingly, the formation of sericite aggregates is often involved in the early or intermediate stages of silicification (Figs 8D, G, H and 9A, F), yet subsequently overprinted by Qtz as this metasomatic process proceeds (Fig. 9G).

Silicification haloes surrounding the GQVs also display by the mylonitic foliation that is recorded in other rock units from the study area, including the GQV Qtz (see above). These mylonites show a moderate dispersion in their structural trend when affecting the Canigó orthogneisses and Costabona monzogranite, although structural analysis shows that an E–W-trend and N-dip direction dominates (Figs 3 and 10B). Mylonitic foliation surfaces affecting GQVs silicified haloes are instead more localised in narrow (10–15-m-thick) mylonitic bands that exclusively follow the trend of the GQVs (Fig. 10B). This could indicate that mylonitisation postdates the GQV formation. However, some outcrops along the GQVs boundary show silicified monzogranite fragments affected by the mylonitic foliation and embedded in an undeformed milky Qtz matrix (Fig. 8E). According to this contrasting evidence, the relative age relationships between GQVs and mylonitic bands cannot be established unambiguously and will be discussed below.

In areas where mylonitisation and metasomatism coexist, different replacement mechanisms can be inferred (Fig. 11A and B). EBSD-based phase maps indicate that albite replaces orthoclase, while Qtz replaces albite and orthoclase, giving rise to pseudomorphs or mineral mixtures within the same parent grain (Fig. 11C). Qtz replacement occurs either in the cores of orthoclase

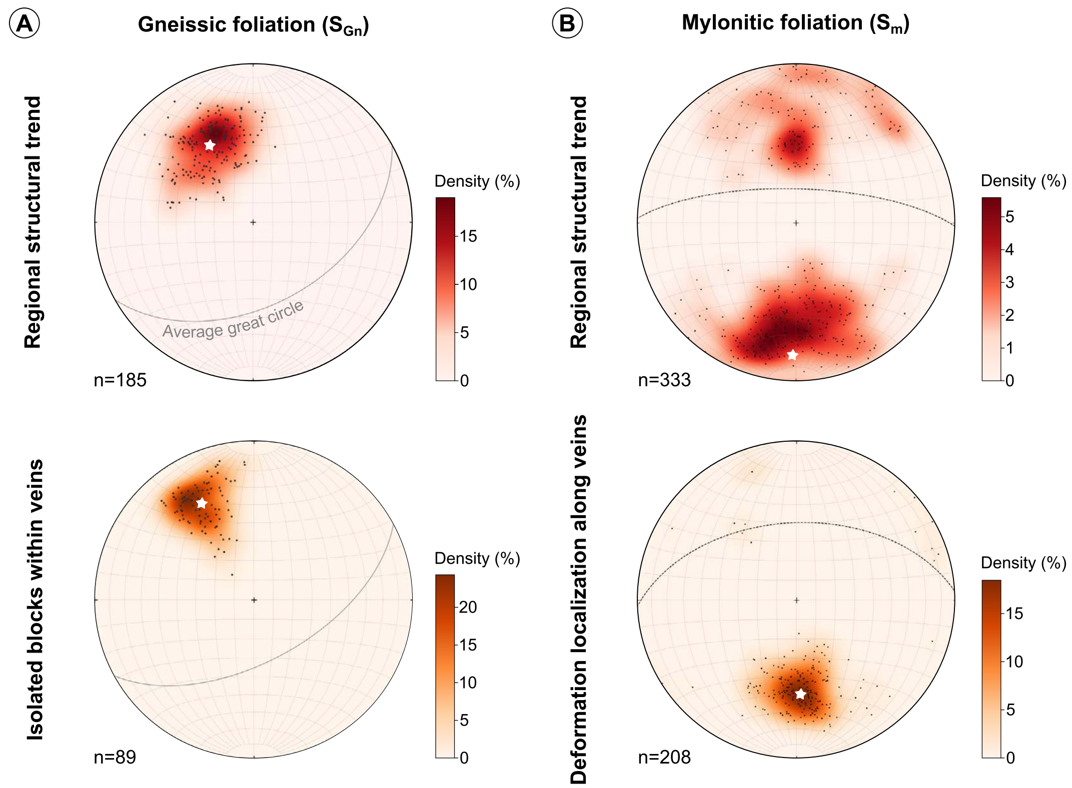

Fig. 10. Equal-area lower-hemisphere stereoplots of the gneissic foliation (S_{Gn}) (A) and mylonitic foliation (Sm) (B) surfaces in the study area. (A) Comparison of the regional S_{Gn} (top) with the S_{Gn} surfaces in the isolated orthogneiss fragments occurring within GQV (bottom) (see Figs 6D and 8C for outcrop examples). (B) Comparison of the regional Sm affecting the Canigó orthogneiss and the Costabona monzogranite (top) with the Sm surfaces heterogeneously developed within the GQV Qtz (bottom); note that poles to planes of Sm affecting GQVs are clustered, indicating a deformation localisation along GQVs.

crystals and, noteworthy, surrounding orthoclase crystals and affecting rims with similar orientation and grain size. This fact suggests that Qtz grains within orthoclase cores are of neoformation and do not represent old veins or inclusions. Grain Reference Orientation Deviation (GROD) maps of replaced and replacing mineral grains suggest that replacement is selective depending on the intra-granular crystal-plastic deformation, as evidenced by high GROD angles in the partially replaced orthoclase crystals and low GROD angles in replacing Qtz and albite crystals (Fig. 11D). Silicification affecting orthoclase is sometimes spatially related to twin planes and grain boundaries (Fig. 11C). Qtz replaces altered orthoclase crystals, which have already experienced a partial to complete replacement by albite and unaltered orthoclase crystals (Fig. 11C and D). In contrast, replacement albite chiefly shows a regular size and appears as patchy accumulations evenly distributed within the orthoclase megacrysts. In all cases, the replacing Qtz and albite do not overgrow the replaced crystals beyond their original grain boundaries, suggesting that replacement took place at constant volume. Moreover, the CPO of replaced and replacing grains indicates a selective orientation inheritance depending on the mineral phases (Fig. 11E and F). The crystallographic orientation was preserved during the replacement of orthoclase by albite, since the orientation of a, b and c axes of the large orthoclase grains is shared by all the small replacing albite grains (Fig. 11F). In contrast to this, the CPO of replacing Qtz grains is not coincident with that of the replaced feldspars, and Qtz c-axis fabrics suggest a combination of basal <a> and prism <a> slip systems in response to deformation under simple shear conditions (Schmid & Casey, 1986; Barth *et al.*, 2010), in agreement with outcrop and microstructural evidence.

Geochemical trends during metasomatism

Bulk-rock compositions of the unaltered Costabona monzogranite and the Canigó orthogneisses have been compared with their alteration products resulting from silicification, feldspathisation and sericitisation, in order to describe the geochemical changes associated with mineralogical transformations occurring during metasomatism (see raw data in González-Esvertit *et al.*, 2024b). Analyses of unaltered Canigó orthogneiss samples published in recent contributions that use similar analytical procedures (Casas *et al.*, 2010, 2024; Navidad *et al.*, 2018; Álvaro *et al.*, 2024) were used for comparison with the metasomatic products addressed in this work (see the NEIGRA database in González-Esvertit *et al.*, 2024b and legend in Figs 12 and 13).

Major elements

The behaviour of major element oxides during metasomatism of the Costabona monzogranite and the Canigó orthogneiss is presented in Fig. 12. Unaltered Canigó G1 and G2 orthogneiss samples range in SiO_2 content from 60 to 78 wt% (Casas *et al.*, 2010, 2024; Navidad *et al.*, 2018; Álvaro *et al.*, 2024; Fig. 12). In contrast, a narrower interval ranging from 68 to 72 wt% is defined by the unaltered Costabona monzogranite samples, as well as by the geochemical analyses already published in Autran *et al.* (1970) and Debon *et al.* (1996). Bivariate plots show consistent linear correlations between SiO_2 and all other major elements of the unaltered

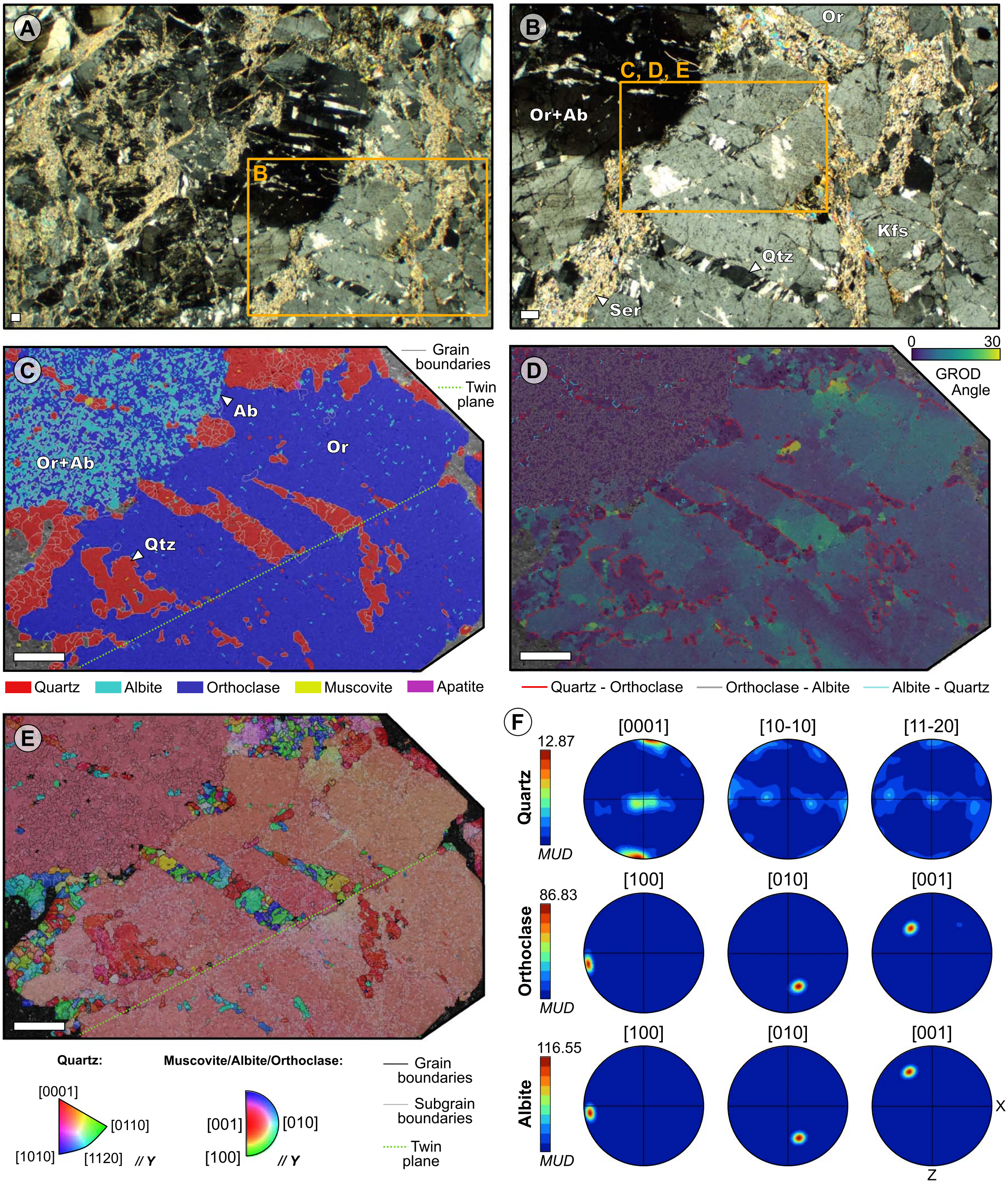

Fig. 11. Representative granite mylonite sample (cut normal to foliation and parallel to lineation) from a silicification halo of a GQV. (A and B) Orthoclase (Kfs), albite (Ab) and Qtz crystals with complex textural relationships; mylonitic foliation wrapping around Qtz and Kfs porphyroclasts is defined by Ser accumulations (XPL). (C) EBSD-based phase map revealing mineral replacement; at the upper left area, Ab replaces Kfs with patchy texture and homogeneous grain size and Qtz partially replaces Ab and Kfs; at the central area, Qtz replaces Kfs along twin planes and grain boundaries, and Ab replaces Kfs incipiently; high-angle grain boundary (HAGB) misorientation threshold for grain reconstruction is ≥10°; low-angle grain boundariy (LAGB) misorientation threshold for subgrain reconstruction is 2–10°. (D) Grain relative orientation deviation (GROD) map showing intra-grain deformation, which suggests that intragranular crystal-plastic deformation is higher in the replaced Kfs crystal and low to moderate in the replacing Qtz and Ab crystals. (E) Inverse pole figure (IPF) map showing grain orientation relative to the main crystallographic axes. (F) Pole figures (one point per grain; lower hemisphere equal-area projections; multiples of uniform density (MUD) coloring) of the principal crystallographic directions (XZ reference frame) of Qtz, Kfs and Ab crystals; Qtz shows a strong crystallographic preferred orientation (CPO) defined by Y-maxima *c*-axis and peripheral maxima *c*-axis fabrics, indicative of prism < a > and basal < a > slip system activation, respectively (see Schmid & Casey, 1986); Ab and Kfs share the same CPO either in the [100], [010] or [001] axes, indicating that replacement took place with orientation inheritance; contrarily, Qtz does not share any CPO with other mineral phases. Mineral abbreviations following Warr (2021).

rocks from this work and from the NEIGRA database, both for the Canigó orthogneisses and for the Costabona monzogranite (González-Esvertit *et al.*, 2024b; dark-grey squares and circles in Fig. 12). Decreasing trends with increasing SiO_2 are obtained for the Al_2O_3, Fe_2O_3, MgO, CaO and TiO_2 diagrams (Fig. 12A–D and G, respectively), which show minor to moderate dispersion. In

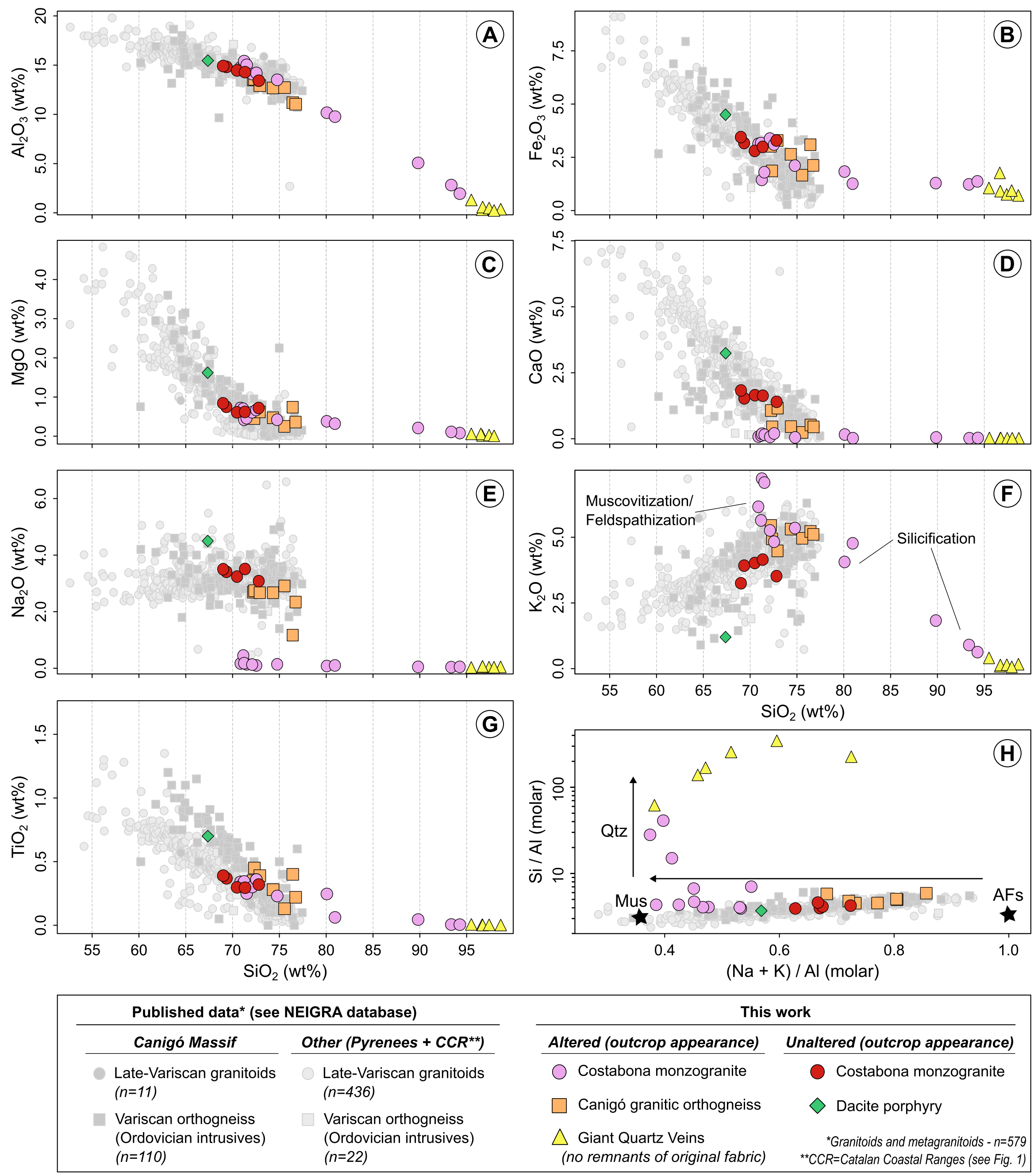

Fig. 12. Bivariate plots of the unaltered and altered samples (coloured symbols) and those compiled in the NEIGRA database (grey symbols; González-Esvertit *et al.*, 2024b). Major oxide concentrations of Al_2O_3 (A), Fe_2O_3 (B), MgO (C), CaO (D), Na_2O (E), K_2O (F) and TiO_2 (G) are plotted against SiO_2 (wt%). (H) (Na + K)/Al vs. Si/Al diagram (Stanley, 2020) showing the geochemical signature of silicification and sericitisation processes; note the logarithmic scale in the Y-axis. Raw data are available in the Supplementary Material 2.

contrast, the K_2O content has a positive correlation with increasing SiO_2 and shows a moderate dispersion (Fig. 12F), whilst the Na_2O (Fig. 12E) yields horizontal trends. The geochemical trends of major elements for the granitic rocks of the Canigó Massif are encompassed in most cases within similar regional patterns defined by other pre-Variscan granitoids from the Pyrenees and the Catalan Coastal Ranges (light-grey squares and circles in Fig. 12). Moreover, unaltered rocks from the Canigó Massif show a similar trend to other Pyrenean Massifs, but being clustered in the lower part of the SiO_2 *vs.* CaO plot because of their lower CaO concentrations (Fig. 12D). The chemical distinction between the Canigó orthogneisses and the Costabona monzogranite is not straightforward if solely based on major elemental concentrations, although orthogneisses have more differentiated compositions, sometimes surpassing SiO_2 concentrations of ca. 75 wt% and higher TiO_2 concentrations. This results in a geochemical trend subparallel to the regional behaviour but shifted towards higher concentrations of both oxides (Fig. 12G).

The altered Canigó orthogneiss and Costabona monzogranite samples show clearly different major elemental compositions and geochemical trends than their precursor rocks (Fig. 12). Samples affected by Si-metasomatism show an increase on SiO_2 and a decrease in all other major elements, which can be correlated with decreasing distances towards GQV outcrops

(Fig. 12, Supplementary Material 2). The trend defined by the silicified Costabona monzogranite samples depicts a semi-continuum towards the GQV Qtz samples, from ca. 75 to ca. 94 wt% SiO_2. These silicified samples show changes in the linear geochemical correlations with SiO_2, from decreasing to sub-horizontal in the SiO_2 *vs*. Fe_2O_3, SiO_2 *vs*. MgO, SiO_2 *vs*. CaO and SiO_2 *vs*. TiO_2 diagrams (Fig. 12B–D and G, respectively), and from increasing to decreasing trend in the SiO_2 *vs*. K_2O diagram (Fig. 12F). The silicified Canigó orthogneiss samples show less increase in SiO_2 concentrations than the silicified monzogranite samples. In the Harker diagrams, they define a cluster with SiO_2 contents ranging from 73 to 77 wt% without geochemical trends in the Fe_2O_3 (Fig. 12B) and K_2O (Fig. 12F) diagrams, negative correlations between SiO_2 and Al_2O_3 (Fig. 12A), Na_2O (Fig. 12E) and TiO_2 (Fig. 12G), and horizontal trends in the MgO (Fig. 12C) and CaO (Fig. 12D) diagrams. Moreover, the slightly increasing K_2O contents with increasing SiO_2 in the silicified orthogneiss samples (Fig. 12F) indicates that silicification is accompanied by moderate sericitisation, as previously reported from field and textural analysis.

Major element behaviour during sericitisation and feldspathisation processes are shown by anomalously high K_2O concentrations compared to the unaltered samples (Fig. 12F). Concentrations of Al_2O_3 in sericitised or feldspathised samples also show a slight increase when compared with the unaltered samples analysed in this work (Fig. 12A). For the analysed samples, feldspathisation is driven by Kfs neoformation and a significant decrease of Na_2O, indicating microclinisation processes (Fig. 12E). Although not recorded in the geochemistry, albitisation involving an enrichment in Na_2O and a depletion in K_2O is also observed in the study area (Figs 7G and 9D). Concentrations of Fe_2O_3, MgO and CaO (Fig. 12B–D, respectively) also show a decrease for the analysed samples that are affected by sericitisation and feldspathisation, whilst TiO_2 concentrations remain uniform for the altered Costabona monzogranite samples and show a slight increase for the altered Canigó orthogneiss samples (Fig. 12G).

GQV samples show SiO_2 concentrations between 95 and 99 wt% (Fig. 12). Minor proportions of Al_2O_3, Fe_2O_3 and K_2O (Fig. 12A, B and G, respectively) likely reflect mica remnants present within GQV Qtz (Fig. 9A, F and G). The alteration of Kfs to muscovite and Qtz (Figs 9B, C and 11C, D) is illustrated by the (Na + K)/Al *vs*. Si/Al diagram (Fig. 12H), where the investigated samples show two continuous trends towards the muscovite and Qtz end-members. No silica addition occurred during muscovite alteration, as evidenced by the horizontal trend alongside decreasing Agpaitic Index. In contrast, silica addition in silicified samples was one order of magnitude larger than Na and K removal in the sericitisation samples (Fig. 12H). Moreover, during silicification, Al, Ca and Na were lost to a greater extent than K. This indicates that small amounts of K were added during silicification or silicification acted upon already feldspathised material, as recorded in vertical trends with a right-directed component with an increasing Agpaitic Index (Fig. 12H).

Trace elements

The behaviour of trace elements during silicification, sericitisation and feldspathisation affecting the Costabona monzogranite and the Canigó orthogneiss is presented in Fig. 13. The unaltered samples of the Costabona monzogranite and the Canigó orthogneiss show an enrichment in large-Ion lithophile elements (LILE) relative to high-field strength elements (HFSE) in the trace element diagrams normalised to the primitive mantle (Fig. 13A and B). Both unaltered rock types show positive anomalies in Pb, K, Sn and Rb and negative anomalies in Nb-Ta, Ti, Ba, P and Sr. Higher values of Cs and Rb with respect to lower values of Tl also represent shifts in the trend of the diagrams (Fig. 13A and B). The only difference between the two unaltered granitic rocks is the negative anomaly of Sr, which is about one order of magnitude lower for the unaltered Canigó orthogneisses with respect to the unaltered Costabona monzogranite samples (Fig. 13A and B). In the chondrite-normalised REE diagrams (Fig. 13C and D), the unaltered granitic rocks show an enrichment of LREE with respect to HREE, as well as relatively flat or slightly concave HREE trends and negative Eu anomalies. Normalised REE values, as well as sample trends, are similar for the Canigó orthogneisses and the Costabona monzogranite with the exception that, for the latter, HREE show a wider compositional range than LREE (Fig. 13C). The obtained trace element diagrams show similarities with other Cambrian–Ordovician magmatic rocks from the Moroccan-SW European margin of Gondwana (Rouergue-Albigeois, Montagne Noire, Southern Cévennes and Mouthoumet massifs; Casas *et al.*, 2024; Álvaro *et al.*, 2024), as well as with other late-Variscan granitoids of the Pyrenees and the Catalan Coastal Ranges (González-Esvertit *et al.*, 2024b). These similarities are further confirmed in individual trace element bivariate plots (Fig. 13E and F), where the unaltered samples plot within the regional trends showing positive correlations in both the Sr *vs*. Eu and Zr *vs*. Ce diagrams (*cf*. Puddu *et al.*, 2019; Álvaro *et al.*, 2020; Liesa *et al.*, 2021).

The altered Canigó orthogneiss and Costabona monzogranite samples show noteworthy differences regarding trace element contents when compared to their precursor rocks (Fig. 13A–F). In the primitive mantle-normalised diagrams (Fig. 13A and B), most elements, including the HFSE, show a progressive depletion there is a wider compositional variation for the altered Costabona monzogranite (Fig. 13A) than for the altered Canigó orthogneisses (Fig. 13B). In some cases, selective enrichment or depletion of some elements is observed depending on the alteration style of the analysed sample, leading to coexisting positive and negative anomalies for a given element in comparison to the unaltered rock equivalent (e.g. Eu, Rb, K, Nd; Fig. 13A and B). In other cases, either positive or negative anomalies present in the unaltered rock types are further emphasised regardless of the alteration type (e.g. Cs, Ba, Sr; Fig. 13A and B), whilst for some elements the anomalies are diminished but still remain slightly positive or negative (e.g. Pb). In the chondrite-normalised diagrams (Fig. 13C and D), the relatively flat pattern and in the HREE trend is preserved irrespectively of the alteration style for both the altered Costabona monzogranite and Canigó orthogneiss samples. Noteworthy, the unaltered Costabona monzogranite samples also show lower contents of W than other granitic rocks from the Eastern Pyrenees.

Depending on the grade of silicification (e.g. incipient, partial or complete), the analysed samples show a progressive depletion in trace elements towards the GQV outcrops, shown as sub-parallel sample trends, which are especially well defined in the HREE (Fig. 13C and D, Supplementary Material 1). This compositional evolution is depicted as a continuum of which the two end-members are represented by the unaltered precursor rock units and by the GQV compositions, as represented for example by REE *vs*. HFSE trends (Fig. 13F). In contrast, samples affected by sericitisation show a noteworthy enrichment in K_2O, Cs, Rb and Tl (Fig. 13A and B), whilst LREE contents remain chiefly similar to those of the unaltered sample equivalents (e.g. La, Ce, Eu; Fig. 13C, E and F). A sample showing feldspathisation is specially enriched in Eu (counteracting the negative anomaly that is recorded in unaltered samples; Fig. 13A and C), as well as in

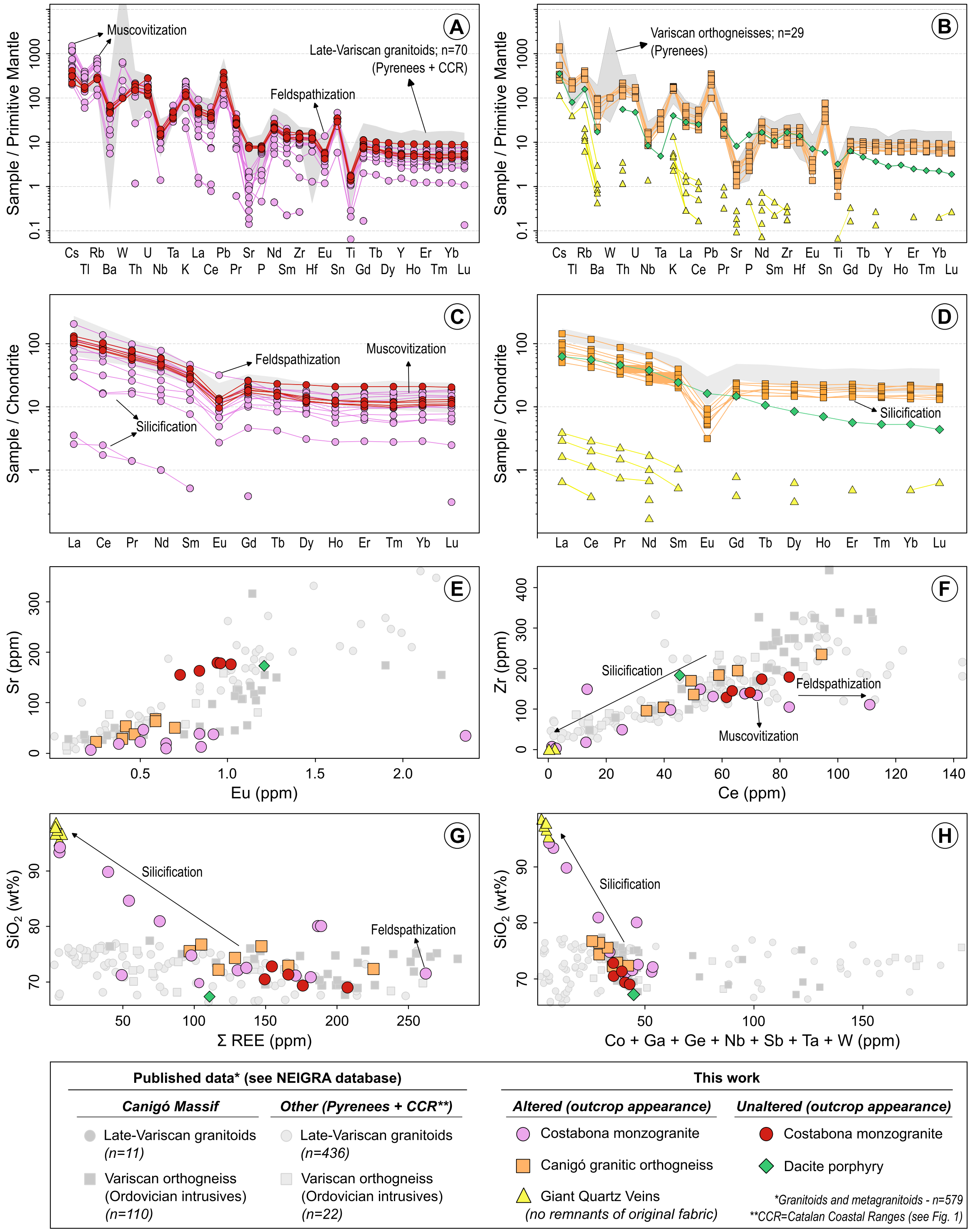

Fig. 13. Trace element compositions of unaltered and altered samples (coloured symbols) and those compiled in the NEIGRA database (grey symbols; González-Esvertit *et al*., 2024b). (A and B) Primitive mantle-normalised extended trace element spider diagrams (Sun and McDonough, 1989) for the unaltered and altered Costabona monzogranite samples (A) and Canigó orthogneiss, dacite porphyry and GQV samples (B). (C and D) C1 chondrite normalised REE patterns (McDonough and Sun, 1995) for the unaltered and altered Costabona monzogranite samples (C) and Canigó orthogneiss, dacite porphyry and GQV samples (D). (E) Sr *vs*. Eu diagram showing the geochemical behaviour of feldspar-bounded elements during alteration. (F) Zr *vs*. Ce diagram showing the geochemical behaviour of HFSE and REE in unaltered samples and their different types of alteration. (G) SiO_2 *vs*. $\sum$REE diagram, showing a progressive depletion of critical elements alongside increasing silicification of the investigated samples. (H) SiO_2 *vs*. non-REE critical elements (Co, Ga, Ge, Nb, Sb, Ta, W).

other LREE (Fig. 13C, E and F). The marked decrease in Sr and other elements that are compatible in feldspar (Fig. 13E) observed in silicified samples can further be related to the breakdown of this mineral (Figs 9A–C and 11C).

Along with silicification, a progressive decrease in the bulk concentration of REE is recorded (Fig. 13G). The total amount of these elements shows its minimum ($\sum = <10$ ppm) in the highly-silicified and GQV samples. Contrary to this, some samples recording feldspathisation show a significant increase in the concentrations of these elements ($\sum = >250$ ppm) (Fig. 13G). Moreover, the non-REE elements identified as critical in >15 criticality studies and/or reports (Co, Ga, Ge, Nb, Sb, Ta, W; see a review in Hayes & McCullough, 2018) show the same depletion trends alongside silicification (Fig. 13H).

Small-scale Si-metasomatism

To investigate the scale of occurrence of the most abundant alteration style in the study area, i.e. silicification (Fig. 3), a cm-scale geochemical profile along a reasonably large and texturally well-characterised sample was carried out (Fig. 14C). The sample, ca. 25 × 20 × 15 cm (height, length and width, respectively), was collected at the boundary between a metre-thick Qtz vein (parallel to the direction of other GQVs in the study area) and its alteration halo, thus representing a small-scale analogue of other, decametre-thick veins present in the Canigó Massif. It contains GQV Qtz at one edge (lower part of panel B1 in Fig. 14B) and a ca. 20-cm long transitional alteration area, along which different minerals become more abundant with increasing distance from the GQV Qtz (see legend in Fig. 14). The sample was cut in seven representative slabs that were analysed following the procedures described above for the rest of the investigated samples. Slabs were cut as large as possible (weights between ca. 200–400 g) to minimise nugget effects during geochemical analyses. Sample portions between the slabs were also cut to prepare 6 'transitional' thin sections, in order to evaluate which mineral phases are present and how do they control the geochemical trends (Fig. 14B and C).

Petrographically, thin sections corresponding to the areas furthest away from the Qtz (B2 and B3 in Fig. 14B) show mineral phases and modal composition estimates typical of granitic rocks and contain xenomorphic Qtz and Kfs with minor idiomorphic biotite, muscovite, sericite and iron oxides (see legend in Fig. 14). As the distance towards the Qtz vein decreases (from top to bottom in Fig. 14B; from C1 to C6 in Fig. 14C), the modal abundance of minerals other than Qtz decreases and mineral replacement textures become the most noteworthy petrographical feature. The first mineral that completely disappears with decreasing distance to the Qtz are Fe-oxides, followed by muscovite and biotite. In the 7 cm immediately adjacent to the GQV Qtz, sericite and Kfs are the only mineral phases present besides Qtz (C5 and C6 in Fig. 14C). The GQV Qtz is entirely formed by inequigranular and partially recrystallised Qtz grains with minor sericite content (Fig. 14C). These textural and mineralogical characteristics are exceptionally well represented by the composition of the investigated sample slabs (Fig. 14A), showing a marked correlation with the distance towards the GQV Qtz. In the Eastern Pyrenees granitoids-normalised diagram, major elements exhibit a partial to complete remobilisation within the 20-cm-wide alteration halo (diagram A1 in Fig. 14A). The enrichment in SiO_2 and depletion in all other major element oxides is well correlated with decreasing distance towards the Qtz. In accordance with textural observations, the feldspar-hosted major elements (K_2O and minor Na_2O and CaO) are, together with the TiO_2, those that show the most pronounced depletion. Moreover, in the primitive mantle-normalised (A2 in Fig. 14A) and the chondrite-normalised diagrams (A3 in Fig. 14A), the progressive depletion of all trace elements is strongly correlated with decreasing distance towards the GQV Qtz, reinforcing the textural observations presented above and further indicating a progressive replacing Si-metasomatism genetically related to GQV occurrence.

DISCUSSION

Element mobility and texture evolution during metasomatism

To evaluate the elemental gains and losses that occurred during feldspathisation, sericitisation and silicification processes, isocon diagrams and their corresponding mass-balance calculations were carried out following the procedures described in Grant (1986, 2005). More details on the isocon method can be found in Supplementary Material 1.

Calculated element gains and losses during feldspathisation and sericitisation affecting the Costabona monzogranite and during silicification affecting the Canigó orthogneiss and the Costabona monzogranite, are provided in Figs 15 and 16, respectively. The studied metasomatic processes suggest a partial to complete remobilisation of all major and trace elements analysed, including those classically considered as immobile, such as Al, Ti and Zr (Figs 15 and 16) (Petersson & Eliasson, 1997; Grant, 2005; Nishimoto & Yoshida, 2010; Nishimoto *et al.*, 2014; Marsala & Wagner, 2016). In fact, it has been demonstrated that Al, Ti and Zr can be mobile at low temperature conditions (Nahon & Merino, 1997; Maggi *et al.*, 2014; Pennacchioni *et al.*, 2016; Han *et al.*, 2023) as witnessed, for example, by Al mobility in bauxite deposits, titanite crystals precipitated within veins, and hydrothermal overgrowths on magmatic zircon cores. For the studied samples, the orders of magnitude of the enrichment/depletion significantly differ between each element (Figs 12, 13A–D and 15A). Moreover, evidence that mineral replacement is the main process controlling this geochemical evolution has been identified at a wide range of scales, from regional (Figs 3, 12 and 13), to sample (Figs 9A and 15) and down to grain scale (Fig. 9B–G and 11). These facts exclude dilution as a factor controlling the geochemical behaviour of the investigated metasomatic styles, suggesting that progressive variations in mineralogy, caused by chemical gradients, were the driving force for the major changes in the whole-rock composition of the altered host rocks. For feldspathisation, there are no spatial patterns of occurrence nor relationships with mesostructures like brittle faults or shear zones in the study area, whilst sericitisation and more often silicification show a very well-defined distribution, often coexisting (Figs 7C and 9F) and being spatially related to the occurrence of mylonitic bands and associated GQVs (Fig. 3; see subsection 5.2). This fact is further confirmed at the microscale: *c*-axis distributions of Qtz replacing albite indicate Qtz deformation under simple shear conditions, in agreement with the relationship between silicification and mylonitisation; by contrast, replacing albite grains show no sign of deformation but an orientation inherited from the replaced orthoclase crystals (Fig. 11).

During feldspathisation (occurring as Kfs episyenitisation in the investigated altered sample) (Fig. 15A and B), a substantial loss of Na_2O can be attributed to the replacement of albite and minor oligoclase by orthoclase. This fact, coupled to the replacement of orthoclase by albite identified through EBSD-based phase mapping (Fig. 11), confirms the spatial coexistence of the two end-members of feldspathisation identified texturally (i.e. albitisation and Kfs episyenitisation; Figs 7F–H and 9A, D, E). The altered rocks of the study area have thus undergone a multi-stage metasomatic history, also involving silicification and sericitisation. Isocon analysis of Kfs episyenites also revealed a gain in other feldspar-bound trace elements (e.g. Eu, Rb, Cs, Tl). These elements have an ionic radius similar to Ba and Sr (difference less than 15%), which are depleted in the altered samples (Fig. 15A and B), as well as to K, which shows a moderate gain. This trace element

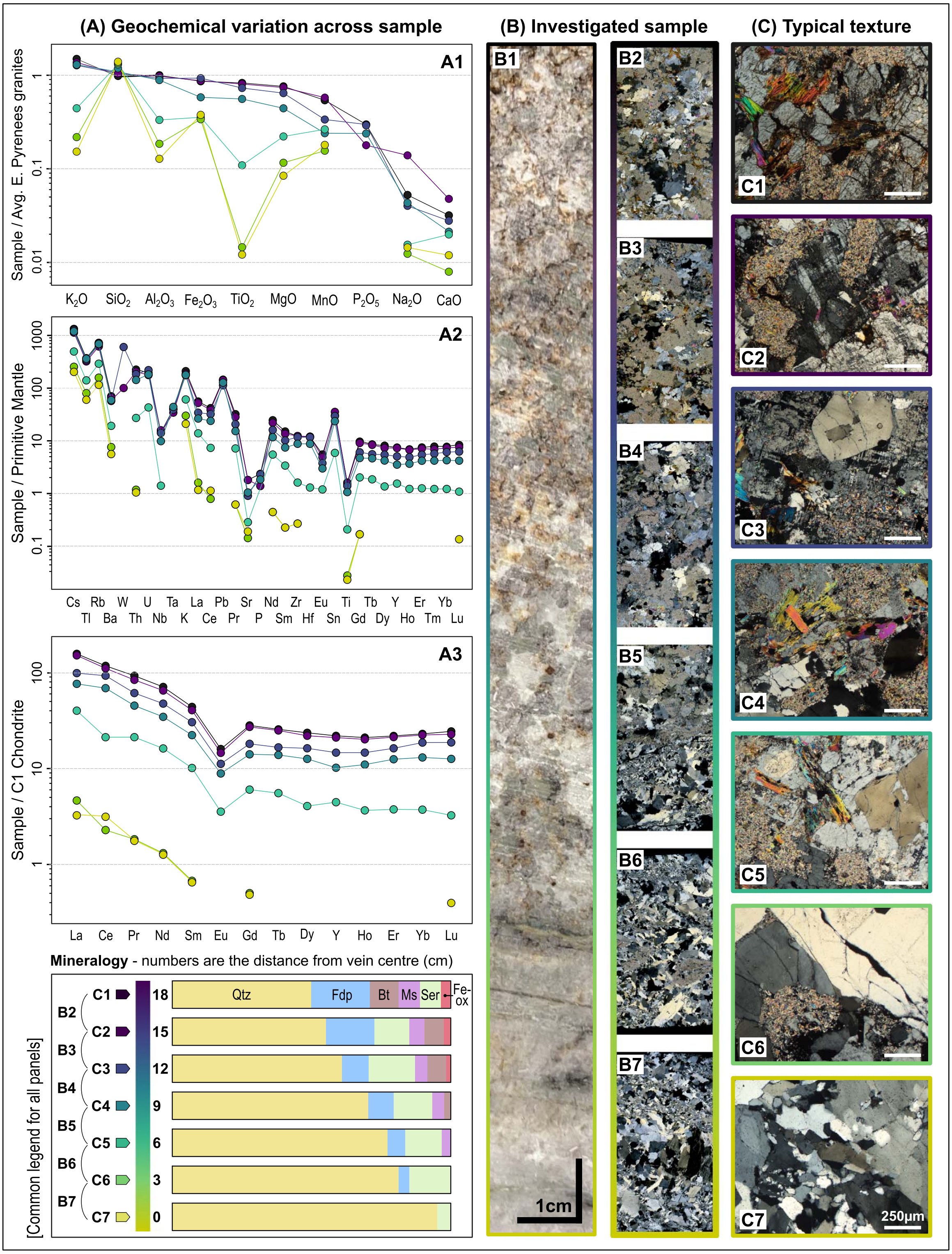

Fig. 14. Evolution of mineral abundance and geochemical composition during silicification at the cm-scale. (A) From top to bottom, major (average Eastern Pyrenees-normalised), trace (primitive mante-normalised), and REE (chondrite-normalised) elemental variation alongside the alteration halo; sample slabs were analysed at different distances (from 18 to 3 cm; each 3 cm) to the vein boundary. (B) The investigated sample (left) and high-resolution thin section scans (right), which are representative of the changes in the mineral assemblage; thin sections represent 'transitional' areas between the analysed slabs; mineral abundance variations of Qtz, Kfs, Bt, Ms, Ser and Fe-oxides (Fe-ox) are quantified through pixel counting and image segmentation. (C) Representative microphotographs (XPL) alongside decreasing distance (from top to bottom) to the vein Qtz. Raw data are available in the Supplementary Material 2. Mineral abbreviations following Warr (2021).

partitioning indicates that the aforementioned elements have behaved as replacing or replaced components through simple (if ionic charges are coincident) or coupled (if ionic charges differ) cationic substitutions within the crystal lattice of newly formed Kfs (Heier, 1962; Ren, 2004; Suikkanen & Rämö, 2019; Morozova *et al.*, 2022). LREE and HREE show, by contrast, different patterns

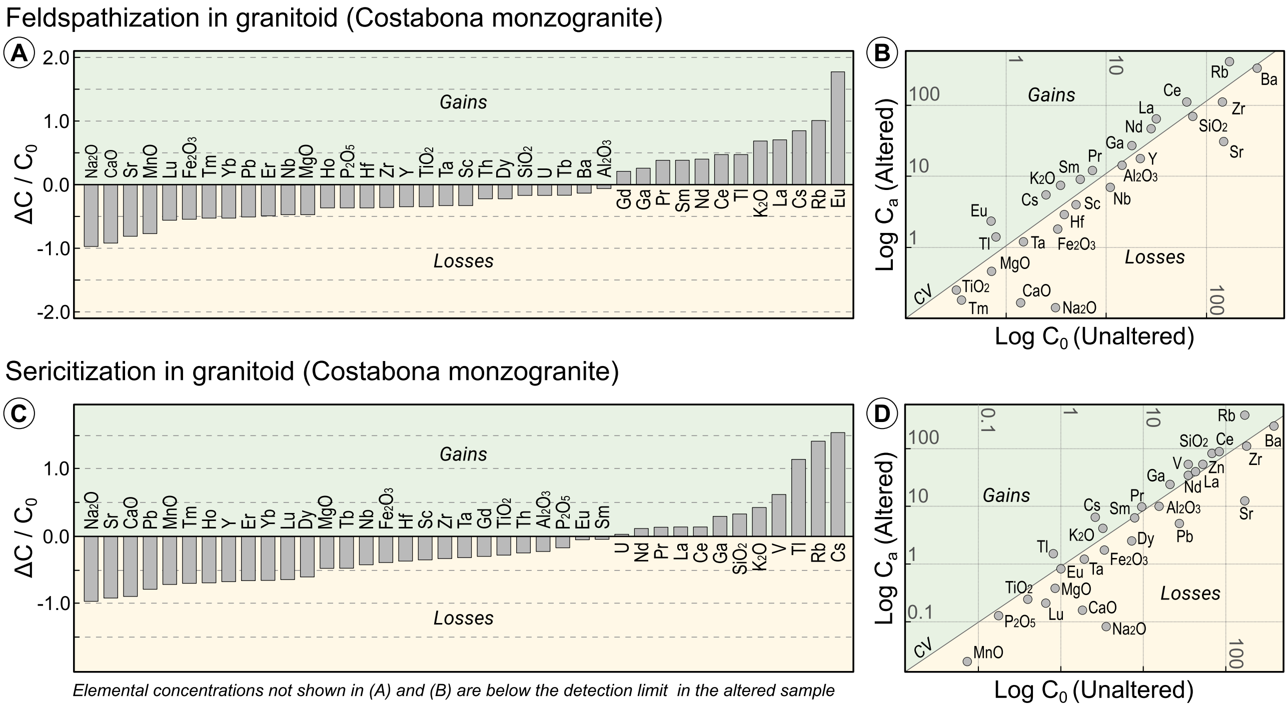

Fig. 15. Relative-concentration-change (left) and Isocon (right) diagrams obtained from geochemical modelling of samples affected by (A and B) feldspathisation (sample RJ21-13) and (C and D) sericitisation (sample RJ21-03A), compared to the typical geochemical composition of the closest unaltered outcrop of Costabona monzogranite (samples RJ21-23 and RJ21-21, respectively). Calculations were made following Grant (1986, 2005) and assuming constant volume (see methods in the Supplementary Material 1 and raw data in the Supplementary Material 2).

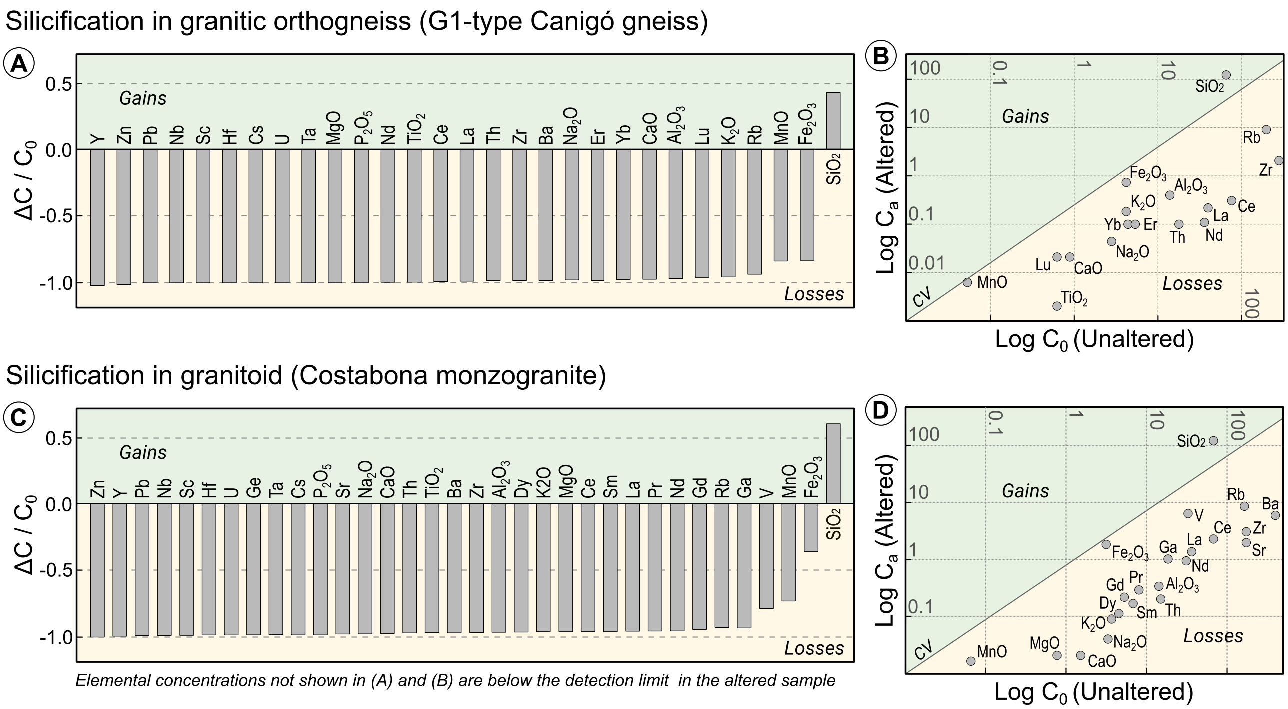

Fig. 16. Relative-concentration-change (left) and Isocon (right) diagrams obtained from geochemical modelling of highly silicified samples from GQVs in (A and B) the Canigó orthogneiss (sample UDT21-14A) and (C and D) the Costabona monzogranite (sample RJ21-03B), compared to the closest unaltered outcrop of each rock type (samples RJ21-18 and CG-20-11, respectively). Calculations were made following Grant (1986, 2005) and assuming constant volume (see methods in the Supplementary Material 1 and raw data in the Supplementary Material 2).

of enrichment and depletion to those generally expected during episyenitisation. A depletion of LREE and an enrichment of HREE are generally reported for different types of episyenites (Petersson & Eliasson, 1997; Hecht *et al.*, 1999; López-Moro *et al.*, 2013; Jaques *et al.*, 2016). However, the investigated feldspathisation process involved an enrichment of LREE and a depletion of HREE in the altered samples (Fig. 13A, C and F).

The isocon analysis of sericitisation (Fig. 15C and D) revealed a significant gain in K_2O and other trace elements that can be accommodated within the white mica structure (Shaw, 1952;

Guidotti *et al.*, 1994a; Guidotti *et al.*, 1994b; Soltani Dehnavi *et al.*, 2019), such as V in the octahedral sheet, and of K, Rb, Tl and Cs cations in the interlayer space (Fleet *et al.*, 2003; Tischendorf *et al.*, 2007; Figs 13A, C and 15C, D). Contrarily, a significant loss of Na_2O, CaO, MnO, MgO, Fe_2O_3, TiO_2, BaO and various HREE is also observed. Depletion of major elements can be related to the change in the composition of micas (i.e. from biotite to muscovite), as well as to simple or coupled cationic substitutions involving Si, Al and Fe^{3+} in the tetrahedral sheet. Noteworthy are the concentration increases in the lithophile trace elements Rb, Cs and Tl, which seem to be common and systematic in metasomatic or hydrothermal white micas occurring in different tectonic settings (*cf.* Alva-Jimenez *et al.*, 2020; Codeço *et al.*, 2021; Benn *et al.*, 2023). Considering elemental gains and losses, as well as the textural features of the investigated samples, sericitisation processes can be mainly attributed to feldspar breakdown (Figs 7C–E and 9A–C) and biotite dehydration (Figs 7F and 8D). The former process causes significant changes in the rock rheology, as it involves the substitution of feldspar, a hard phase with brittle behaviour up to 450–500°C (Voll, 1976; Simpson, 1985), by white mica, a much softer phase that is easily deformed by basal glide and dissolution-precipitation creep (Hunter *et al.*, 2016; Tokle *et al.*, 2023). Accordingly, sericitisation may have played a role in strain localisation and the development of shear zones throughout the study area, directly affecting the strength of the sericitised rocks and the deformation behaviour of other mineral phases (Gueydan *et al.*, 2003; Menegon *et al.*, 2008; Toy *et al.*, 2008; Finch *et al.*, 2020). In fact, textural evidence of silicification overprinting sericitisation was found (Figs 7G, H and 9F, G), which may explain the spatial relationship between sericitised and silicified sectors with the regional-scale shear zones occurring throughout the study area (Fig. 3). Sericitisation could, therefore, represent one of the mechanisms preconditioning strain localisation and can be genetically linked to the identified GQVs and mylonitic bands of the southern part of the Canigó Massif. In the northern area of the massif, Casas (1984) also pointed out that progressive replacement of Kfs and plagioclase was related to the formation of thick (200–500 m) mylonitic bands formed by Qtz, muscovite and calcite in the Font Pedrosa-Nyer area.

Moreover, the substantial loss in MgO, FeO and TiO_2 during feldspathisation (Fig. 15A and B) and sericitisation (Fig. 15C and D) can be further related to the biotite loss identified at the outcrop and thin section scale (Figs 7F and 8D). Reactions leading to biotite dehydration are well known from natural and experimental data at high temperature (amphibolite and granulite facies conditions), under which they favour partial melting and the formation of migmatites (Rutherford, 1969; Graphchikov *et al.*, 1999; Barbey, 2007; Imayama *et al.*, 2019). However, the low-temperature breakdown of biotite has been the subject of much less investigation despite being known to represent, for example, a significant source of water (Weisheit *et al.*, 2013). Tulloch (1979) and Eggleton & Banfield (1985) were the first who described low-temperature (300–350°C) biotite breakdown, often coupled to the alteration of plagioclase to sericite and to the formation of chlorite, muscovite, Kfs and titanite crystals. In this framework, Mg, Ti, Fe cations would be conserved within the newly formed mineral assemblage. However, these minerals are not present in the altered rocks investigated here and, therefore, these reactions cannot explain the loss of MgO, FeO and TiO_2 as seen in isocon modelling (Fig. 15A and B). Holness (2003) concluded that lenses of pure Kfs, affected by variable degrees of albitisation, were formed through low-temperature (<300°C) biotite-breakdown reactions. Moreover, Weisheit *et al.* (2013) used volumetric calculations based on alteration mapping and mineral phase proportions to infer that 10.8 km^3 of fluid would be produced by the partial (50%) biotite dehydration of 720 km^3 of schists and gneisses containing 30% of biotite. According to this, the authors suggested that the H_2O release from biotite breakdown was, among others, one of the main fluid sources responsible for the formation of the Hidden Valley megabreccia in South Australia. The reduced H_2O activity needed to trigger biotite dehydration was, according to Weisheit *et al.* (2013), favoured by high-salinity fluids (Bakker & Elburg, 2006). In the study area, identifying whether biotite dehydration during feldspathisation or sericitisation processes (Figs 7C, 8D and 9A–C) may have been a significant fluid source for silicification would depend on the relative ages of the three metasomatic processes, which are unknown. However, the absence of chlorite in either feldspathised, sericitised or silicified rocks of the study area and the high salinity recorded by fluid inclusions within GQVs (Ayora & Casas, 1983; González-Esvertit *et al.*, 2025b), may favour this hypothesis. In this framework, silicification processes involving a gain in Qtz could have partially been sourced by biotite dehydration, releasing water, coupled to Qtz dissolution in surrounding rocks and sericitisation of Kfs, releasing silica in the form of SiO_2 and orthosilicic acid, respectively. Moreover, the ferromagnesian elements released from biotite dehydration may have formed the Fe-oxides present in the altered areas (Figs 9B, E and 14B) or also incorporated into the fluid phase and leached away from the study area.

The geochemical behaviour of some elements, however, does not follow the expected trends (Fig. 15). For example, a gain in Al_2O_3 may be expected from either feldspathisation or sericitisation (Pennacchioni *et al.*, 2016; Suikkanen & Rämö, 2019), since Al_2O_3 is present in the crystal structures of Kfs and sericite. The unexpected Al_2O_3 loss can be attributed to prior metasomatic reactions, involving other mineral phases, which may have been texturally overprinted by the studied alterations that only left a geochemical fingerprint, but may not be detected petrographically. Accordingly, the net balance of such reactions would be difficult to reconcile with the mineralogy considering the multi-stage metasomatic history registered in the studied rocks.

In addition to the sericitisation and feldspathisation evaluated through isocon modelling, an enrichment in albite was also identified through textural analysis (Figs 7G and 9D) but not detected in geochemical analyses. The presence of chessboard albite suggests replacement of Kfs under solid-state albitisation (Moore & Liou, 1979; Charoy & Pollard, 1989). In this framework, potassium released from the Kfs breakdown could have reacted with aluminous silicates to form white mica, thus potentially triggering subsequent sericitisation. The Balaig metasediments further show noteworthy mineralogical changes in some areas, where the unaltered micaschists progressively acquire a chiefly polygonal fabric that is spatially associated with the gradual disappearance of micas. Although the final product of this alteration is a quartzofeldspathic rock that resembles a granite, no evidence for partial melting, nor high temperature porphyroblasts are visible where this alteration style crops out. These observations suggest that it took place under solid-state, low-to-medium temperature conditions.

Are GQVs really veins?

Irrespective of their size, mineral veins are understood and defined in different manners depending on the discipline of Earth or Material Science under which they are investigated. One of the most accepted definitions states that veins are mineral aggregates that precipitated from a fluid in dilational sites (Bons *et al.*, 2012).

This definition has genetic implications and thus excludes small-scale igneous dykes and leucosomes, where minerals crystalise from a melt, as well as replacement veins, where dilation is not necessarily present (Fletcher & Merino, 2001). Veins *sensu stricto* are, accordingly, intimately related to fracture mechanics (Durney & Ramsay, 1973; Ramsay, 1980; Passchier & Trouw, 1996; Bons, 2000; Koehn *et al.*, 2005; Bons *et al.*, 2012, 2022).

GQVs are the most noteworthy feature in the study area (Figs 2–4), and their origin and significance are far from negligible. Similar structures have been identified in many tectonic settings worldwide, sometimes associated to ore deposits, and being hosted by rocks of different age and composition: Bundelkhand craton (Central Indian Shield, India; Pati *et al.*, 2007; Slabunov & Singh, 2022), South Armorican Massif (NW France; Lemarchand *et al.*, 2012), Tyndrum–Dalmally area (Grampian Highlands, N Scotland; Tanner, 2012), Qinling–Dabie belt (W Henan Province, China; Gao *et al.*, 2013), Heyuan Fault Zone (SE China; Tannock *et al.*, 2020), Birimian terranes (Ashanti Belt, S Ghana; Oberthür *et al.*, 1997), Veta Madre (Guanajuato Mining District, Mexico; Moncada *et al.*, 2012) Kirkland, Porcupine and Hemlo Superior provinces (SE Canada; Jia & Kerrich, 2000), Mother Lode belt, California Western Sierra (W United States; Sibson, 2020), Dharwar Craton (Kolar and Gadag greenstone belts, India; Mishra *et al.*, 2018), Broken Hill Inlier (New South Wales, Australia; Bons, 2001), Eastern Andean Cordillera (Bolivian Tin Belt, SW Bolivia; Ahlfeld, 1967), among others. However, their fluid and silica sources and transport modes, as well as the time span required for their formation, remain debated hitherto (Jia & Kerrich, 2000; Bons, 2001; Sharp *et al.*, 2005; Lemarchand *et al.*, 2012; Tannock *et al.*, 2020; Rout *et al.*, 2022; González-Esvertit *et al.*, 2022b, 2024a).

In some of the aforementioned regions, GQVs show clear features of being either genetically related to fluid flow *through* previously opened fractures or *with* opening (fluid-filled) fractures, involving dilation and advective fluid transport (Sibson *et al.*, 1975; Yardley, 1983; Bons, 2001; Hilgers *et al.*, 2004). The evidence include, among others, very limited (or absent) host-rock alteration, abundant crack-seal structures, microstructures indicating volume loss in the host rocks, net boundaries between GQVs and host rocks, and absence of significant deformation within the vein Qtz (Bons, 2001; Tannock *et al.*, 2020; Rout *et al.*, 2022). Therefore, GQV Qtz in these cases was precipitated from a fluid in dilational sites, forming veins *sensu stricto.* The GQVs investigated here, however, show contrasting field, microstructural, geochemical and crystallographic features indicating that Si-metasomatism, and its associated replacive silicification, was responsible for their formation:

- Outcrop textural features: (1) relict grains and traces of host-rock foliations and lineations within the GQV Qtz (Figs 6D, 8A, C and 10A); (2) feldspar megacryst pseudomorphs formed by Qtz in areas where the Costabona monzogranite is close to GQVs (Fig. 8B); (3) continuity of ghost traces of the gneissic foliation towards the core zones of GQVs (Figs 6D and 8A); (4) pervasive silicification forming symmetric alteration haloes that follow the structural trend of GQVs (Figs 3 and 8G, H). These pieces of evidence have also been reported in other sectors of the Pyrenees where GQVs are hosted by Palaeozoic metasediments and Cenozoic sedimentary rocks (González-Esvertit *et al.*, 2022b, 2023, 2024a).
- Outcrop structural features: (1) diffuse GQV boundaries, where it is not possible to determine a specific GQV-host rock contact because the transition is progressive (Fig. 8F–H); (2) host-rock fragments isolated within the GQV Qtz that show planar mesostructures with the same structural trend (Figs 6D, 8C, E and 10A). These trends are, in turn, equal to the regional structural trend, indicating that neither transport nor rotation of the fragments has occurred (Fig. 10A).
- Microstructural evidence: (1) increasing proportions of xenomorphic Qtz aggregates with decreasing distance towards the GQVs (Figs 8A and 14B, C); (2) isovolumetric replacement of Kfs and muscovite crystals and sericite aggregates by Qtz (Figs 8A, B and 9F, G); (3) synchronous silicification and mylonitisation that would explain the observed Qtz *c*-axis fabrics (Fig. 11F), generally attributed to high greenschist–amphibolite facies conditions (>400°C; Toy *et al.*, 2008), which clash with other evidence of low-T GQV formation and deformation found in the studied samples (lack of high-T mineral phases, brittle behaviour of Kfs and fluid inclusion data from Ayora & Casas (1983) and González-Esvertit *et al.* (2025b) (Fig. 9B and C). In this scenario, the water-weakening effect could have enabled an easier dislocation glide and diffusion at lower T, allowing mylonitic deformation to localise along GQVs that apparently represent a harder phase within the (mica-rich), softer Costabona monzogranite (Figs 3 and 10B).
- Spatially resolved whole-rock geochemistry, at the m-km scale: progressive enrichment of SiO_2 and depletion of all other major and trace elements with decreasing distance towards the GQVs (Figs 12 and 13), as further confirmed by mass-balance modelling trough the isocon method in the silicified Canigó orthogneiss (Fig. 16A and B) and Costabona monzogranite (Fig. 16C and D). The elements lost during silicification can be related to biotite dehydration and the replacement of muscovite and feldspar by Qtz, as identified texturally in outcrops and thin sections (Figs 7C, 8A, B, D and 9A, F, G). Moreover, the trends in Figs 12 and 13 further suggest that, for some samples, silicification processes acted upon already feldspathised rocks.
- Spatially resolved whole-rock geochemistry and comparative point counting on thin sections, at the mm–cm scale: (1) Gradual transition within ca. 20 cm from a granite-looking rock to almost pure Qtz mineral aggregate. This is exposed as a progressive change in the relative abundance of mineral phases and their associated geochemical change in sample traverses, which correlate with the distance towards the GQV boundary (Fig. 14).
- EBSD-based phase maps and CPOs: (1) replacement of orthoclase and albite by Qtz along twin planes and grain boundaries at the μm scale (Fig. 11A and B), as well as below the resolution of the optical microscope (Fig. 11C); (2) selective replacement depending on intra-granular crystal-plastic deformation of the pre-existing, replaced grain (Fig. 11D); (3) absence of orientation inheritance in the replacing Qtz, probably due to the aforementioned synchroneity between silicification and mylonitisation (Fig. 11E and F).

These pieces of evidence of mineral replacement processes, as well as the strong fluid–rock interactions that they involve, seem incompatible with fast advective fluid transport through previously opened fractures or by 'burbs' of ascending fluids with mobile hydrofractures (Bons, 2001; Bons *et al.*, 2022). However, it is also difficult to identify and quantify, if silica was derived locally. Given that the rocks in the study area are intrinsically rich in SiO_2, a very limited silica loss occurring in a significant rock volume would only result in minor changes of the whole-rock composition and could even be below the detection limit of the analytical methods used. The total amount of silica required for the formation of the GQVs in the study area according to the current vein formation models can be roughly estimated using cartographic constraints (GQV width 'W_{GQV}', length 'L_{GQV}' and height 'H_{GQV}') and considering a Qtz density of 2.65 g/cm^3. Assuming a vertical extent of 1/3 of the horizontal one ($H_{GQV} = \frac{1}{3}L_{GQV}$) for those veins with $L_{\mathbf{GQV}} < 2000$ **m** and of 1000 m ($H_{\mathbf{GQV}} = 1000$) for those larger veins, the volume of each GQV can be calculated as (see GQV heigh and width estimates in Ayora & Casas, 1983 and González-Esvertit *et al.*, 2022a, respectively):

$$V_{GQV} = \frac{4}{3} \times \pi \times (W_{GQV} \times L_{GQV} \times H_{GQV}) \quad (1)$$

and the Qtz mass (m_{qtz}) precipitated in the study area, forming n GQVs of known volume, can be obtained by:

$$m_{qtz} = \left(\sum nV_{GQV}\right) \times 2.65 \quad (2)$$

A total amount of ca. 4.2 · 10^{12} kg of Qtz is inferred when considering all the GQVs in the study area; from these, ca. 2 · 10^{12} kg correspond to the largest GQV (the 11 km-long Esquerdes de Rojà vein; Fig. 3). This estimate neglects the partially silicified areas that developed outside GQVs, which, if considered, would have resulted in an even higher value of m_{qtz}. The total fluid budget needed to transport that silica and form the studied GQVs is, however, difficult to estimate due to the unknown fluid salinity and pH, and the various possible forms by which silica can be transported (e.g. dissolved Qtz or amorphous silica). Depending on these constraints, the silica solubility can vary up to orders of magnitude for the same temperature conditions (Pan *et al.*, 2021; McNab *et al.*, 2024). A rough approach may be calculated from experimental and theoretical Qtz solubility determinations (Staude *et al.*, 2009). Assuming a fluid temperature of 250°C and a Qtz solubility in water of 0.25 kg/m^3, ca. 2 · 10^{13} m^3 of fluid would be needed to form the investigated veins. This is, for comparison, ca. 3.5 times the water volume of Lake Michigan in the United States or ca. two times the water volume of the Lake Malawi in southern Africa (van der Leeden *et al.*, 1990; Cael *et al.*, 2017). However, this fluid volume could be orders of magnitude higher or lower depending on the aforementioned constraints, and more knowledge on the physicochemical properties of the fluid would be needed in order to accurately estimate the exact amount.

An advective fluid transport mechanism must be invoked, besides the replacing Si-metasomatism, in order to explain at least the crack-seal small-scale Qtz veins forming ca. 10% of the GQVs that are present in the study area. Therefore, we suggest that the combination of extensive host-rock replacement through Si-metasomatism with intermittent advective fluid pulses are the most reliable explanation for the observed field, microstructural and geochemical features of the investigated GQVs. A similar combination of diffusive and advective fluid transport (Dissolution-Diffusion–Advection Model; Rout *et al.*, 2022) has already been proposed for the giant Qtz reef system at the Bundelkhand Craton, supported by textural, fluid inclusion and geochemical modelling evidence. However, these authors assume extensional fracturing in order to explain why the reefs are developed in a given site. In the Canigó Massif, the formation process of GQVs can be invoked as a progressive accumulation of silica coeval with mylonitisation, which would have been governed by chemical and pressure gradients probably caused by that mylonitisation (Banerji, 1981; Goncalves *et al.*, 2012; Odlum & Stockli, 2020).

Most of the exposed areas generally understood as part of the GQVs in the Pyrenees are, therefore, not veins *sensu stricto* but metasomatic products where the original fabrics and features of precursor rocks have been overprinted during coupled deformation and replacive Si-metasomatism. In the same manner that an albitite, a metasomatic monomineralic rock composed of albite, can be formed through metasomatism from a precursor Qtz-felspathic rock (Boulvais *et al.*, 2007; Poujol *et al.*, 2010; Petersson *et al.*, 2012), a comparable petrogenetic history may be invoked for a vein-shaped structure entirely composed of Qtz. This would further explain the replacement features and alteration haloes found in other GQVs of the Pyrenees hosted by different rock types (González-Esvertit *et al.*, 2022a, 2022b, 2024a). In these scenarios, the shape of Qtz accumulations would mostly be determined by the type of deformation mesostructures that governed silica concentration. For the studied cases, these structures have resulted in lenticular vein shapes because silica concentration was governed by shear zones. The term GQV should not have, accordingly, genetic implications because, as suggested by incipient silicification areas with 'pod' morphologies, shape is only the result of the driving force leading to silica concentration. This fact highlights the need of further studies in other settings worldwide where GQVs, or pseudo-GQVs, are present, as well as the importance of considering replacement processes when dealing with the formation mechanisms of veins with different mineral assemblages. In the Bundelkhand Craton, for example, the term *reef* instead of *vein* is often used for these structures in order to apply a non-genetic, geomorphic nomenclature (Rout *et al.*, 2022).

The implications of the results here presented are further relevant for two currently debated issues: (1) the differential stresses that may, or may not, be caused by mineral reactions (Carmichael, 1987; Fletcher & Merino, 2001; Tajčmanová *et al.*, 2015; Plümper *et al.*, 2022) and (2) the understanding of fluid, heat and mass transfer leading to changes in the physicochemical properties of the Earth's crust and lithospheric rheology, which further involves the interplay between Qtz cementation and the seismic cycle (Miller, 2013; Saishu *et al.*, 2017; Williams & Fagereng, 2022). For the former, the isovolumetric character of the replacement reactions associated to the investigated metasomatic processes are noteworthy. Solid-volume change (ΔVs) during mineral reactions has either been invoked as non-existent (i.e. isovolumetric replacement *sensu stricto*, preserving the external dimensions of the parent grains; Fletcher & Merino, 2001; Canals *et al.*, 2019), positive (i.e. volume increase, generating high-magnitude differential stresses; Jamtveit *et al.*, 2009; Plümper *et al.*, 2022) or negative (i.e. volume decrease, generating porosity; Pedrosa *et al.*, 2016; Weber *et al.*, 2021). When ΔVs is positive, these reactions may infer high-magnitude stresses that induce rock fracturing (Jamtveit *et al.*, 2009; Kelemen & Hirth, 2012), plastic deformation and even represent the first step toward crustal seismicity (Plümper *et al.*, 2022). In contrast, when mineral reactions occur associated to negative ΔVs, nanoporosity may be generated further inducing nanofluidic transport, enhancing metamorphic fluid flow and fluid-mediated mineral transformation reactions (Plümper *et al.*, 2017). Notwithstanding, these processes are not expected during mineral replacement reactions at constant volume, such as those reported in the present work at the mm—μm scale. Further investigation is needed in order to elucidate whether the volume of replaced and replacing minerals during the investigated processes is still constant, or not, at the sub-micron scale. On the other hand, the long-lasting timescales of GQV formation elucidated in this work are difficult to reconcile with the timescales of strength recovery of rocks during interseismic periods and seismogenic depths and temperatures. This agrees with the absence of geological evidence of slip-related mechanisms (e.g. pseudotachylytes) spatially related to silicification sectors in the study area. Other Qtz precipitation processes occurring at earthquake nucleation temperatures (150–350°C) have also been questioned as reliable mechanisms for strength recovery between earthquakes (see a review in Williams & Fagereng, 2022).

Finally, if GQVs are assumed to be mostly formed by mineral replacement, it is worth to ask where the elements lost during their formation (Figs 15 and 16) now reside. The volume of elements in the pre-existing rocks, now replaced by Qtz, would be in the order of 10^9 m^3 if only the silicification areas leading to GQV formation are considered, or significantly higher if muscovitisation, feldspathisation and incipient silicification areas are also considered. From this volume, a remarkable fraction could correspond to elements with economic importance, such as REE (Fig. 13G) and other critical elements (Fig. 13H) (c.f. U.S. Geological Survey, Department of the Interior, 2022). The chemical behaviour and scales of occurrence of metasomatism in barren systems are often overlooked because their low economic potential, although they are as genetically significant as economically important ones and sometimes better exposed. Accordingly, the comparative appraisal of barren and mineralised areas involving Si-metasomatism can help to elucidate how the physicochemical conditions vary between mineralised and non-mineralised systems and, therefore, to unravel which are (and which are not) the petrogenetic constrains needed for a metasomatic ore deposit, as previously investigated for other types of ore deposits (Hendry *et al*., 1985; Gregory *et al*., 2019). In the studied area, for example, the element loss and the fluid surplus after silicification must have gone somewhere trough advective transport, producing more fluid–rock interaction and mineral precipitation in other over-enriched areas in the Pyrenees. These areas, some of them probably still buried or already eroded, may deserve further attention not only in terms of ore deposit petrogenesis, but also due to their potential relationship with Mg-metasomatism expressed through dolomitisation, talcification and chloritisation processes throughout the Pyrenees.

CONCLUDING REMARKS

Here, we have evaluated, across scales, the multi-metasomatic history of granitoid rocks cropping out in the Canigó Massif (Eastern Pyrenees). Macro- (km), meso- (m–cm) and micro-scale (μm) evidence, based on outcrop and thin section characterisation, EBSD and whole-rock geochemistry, provided new insights into the mineral replacement reactions and geochemical behaviour during feldspathisation, sericitisation and silicification processes. The NEIGRA database further allowed the geochemical comparison of altered rocks with other unaltered granitoid samples from the basement rocks of the Pyrenees and the Catalan Coastal Ranges. Overall, all major and trace elements behave as mobile during either silicification, feldspathisation and sericitisation processes here investigated. Results suggest that silicification is the dominant metasomatic process and was related to regional-scale shear zones. Relict grains and fabrics of precursor rocks within veins, a progressive depletion of all major and trace elements but silica along decreasing distances towards veins and the localisation of mylonitic deformation along veins, are multi-scale witnesses of GQV formation through mineral replacement coupled to mylonitisation. Accordingly, it is suggested that these structures are not veins *sensu stricto* but products of Si-metasomatism leading to strong host-rock alteration; that is, pseudo-GQVs. Results presented here have major implications for our understanding of the scale and geochemical behaviour of metasomatic reactions and their associated ore deposits, as well as for the kinetics of mineral replacement reactions inferring changes in the physicochemical properties of the Earth's crust.

SUPPLEMENTARY DATA

Supplementary data are available at *Journal of Petrology* online.

ACKNOWLEDGEMENTS

We acknowledge the insightful and constructive comments and suggestions provided by Samuele Papeschi and one anonymous referee, as well as editorial guidance by Valentin Troll and Georg Zellmer. We are thankful to Carles Ayora for his help during fieldwork at the Esquerdes de Rojà area, to Guillem Gisbert for his insightful comments that contributed to improving an earlier version of this manuscript, and to John Still for his assistance during SEM-EBSD data acquisition at the ACEMAC Facility (University of Aberdeen). We acknowledge Oxford Instruments for providing a Student Licence for the AZtecFlex software package. This research was funded by the DGICYT Projects PID2021-122467NB-C22, PID2021-125585NB-I00 and PID2022-139943NB-I00 (MCIN/AEI/FEDER-UE/10.13039/501100011033), PID2020-118999GB-I00 (MCIN/AEI/10.13039/501100011033), the 'Modelització Geodinàmica de la Litosfera' (Generalitat de Catalunya, 2021 SGR 00410), 'Sedimentary Geology' (Generalitat de Catalunya, 2021 SGR 00349) and 'GEOXiS' (Generalitat de Catalunya, 2021 SGR 00262) Consolidated Research Groups and the VolcPeG Research Group. EGE acknowledges the funding provided by the Geological Society of London (GSL) Student Research Grants, the PhD grants funded by Generalitat de Catalunya and the European Social Fund (2021 FI_B 00165 and 2022 FI_B1 00043). CPT acknowledges the PhD grant 2021 FISDU 00347 funded by Generalitat de Catalunya. EGR acknowledges funding provided by the Spanish Ministry of Science, Innovation and Universities ('Ramón y Cajal' fellowship RYC2018-026335-I). CA is grateful to the GEOXis Reseach Group (2021 SGR 00262) and the projects PID2020-117332GB-C21 (USAL) and PID2020-117332GB-C22 (UCM) funded by MCIN/AEI/10.13039/501100011033.

Data availability

Extended methods and detailed rock descriptions are provided in the Supplementary Material 1. Geochemical data included in this paper is provided in the Supplementary Material 2 and has been uploaded to the Open Access digital repository DIGITAL.CSIC (last access: November 2024): https://doi.org/10.20350/digitalCSIC/16236. Whole-rock major and trace element analyses of the investigated samples are also available at the EarthChem data repository: https://doi.org/10.60520/IEDA/113400.

REFERENCES

Adams, F. D. (1901). The excursion to the Pyrenees in connection with the eighth international geological congress. *The Journal of Geology* **9**, 28–46. https://doi.org/10.1086/620878.

Aguilar, C., Liesa, M., Castiñeiras, P. & Navidad, M. (2014). Late Variscan metamorphic and magmatic evolution in the eastern

Pyrenees revealed by U–Pb age zircon dating. *Journal of the Geological Society* **171**, 181–192. https://doi.org/10.1144/jgs2012-086.

Ahlfeld, F. (1967). Metallogenetic epochs and provinces of Bolivia: the tin-province (part I) the metallogenetic provinces of the altiplano (part II). *Mineralium Deposita* **2**, 291–311. https://doi.org/10.1007/BF00207022.

Alva-Jimenez, T., Tosdal, R. M., Dilles, J. H. *et al.* (2020). Chemical variations in hydrothermal white mica across the Highland Valley porphyry Cu-Mo District, British Columbia, Canada. *Economic Geology* **115**, 903–926. https://doi.org/10.5382/econgeo.4737.

Álvaro, J. J., Sánchez-García, T., Puddu, C. *et al.* (2020). Comparative geochemical study on Furongian–earliest Ordovician (Toledanian) and Ordovician (Sardic) felsic magmatic events in South-Western Europe: underplating of hot mafic magmas linked to the opening of the Rheic Ocean. *Solid Earth* **11**, 2377–2409. https://doi.org/10.5194/se-11-2377-2020.

Álvaro, J. J., Sánchez-García, T. & Casas, J. M. (2024). The Cambrian atlas – Ossa-Morena – Northarmorican rift, West Gondwana: along- and off-axis, stratigraphic and volcano-tectonic patterns. *Geological Society, London, Special Publications* **542**, SP542-2023-24. https://doi.org/10.1144/SP542-2023-24.

Autran, A. & Guitard, G. (1957). Sur le granite de Mont-Louis (Pyrenees-Orientales). *Bulletin de la Société Géologique de France* **S6-VII**, 245–270. https://doi.org/10.2113/gssgfbull.S6-VII.1-3.245.

Autran, A. & Guitard, G. (1968). Carte géologique détaillée de la France à 1/80.000: Prades. *BRGM Service de la carte Géologique de France*.

Autran, A., Fonteilles, M. & Guitard, G. (1970). Relations entre les intrusions de granitoides, I'anatexie, et le métamorphisme regional considertes principalment du point de vue de l'eau: cas de la Chaine Hercynienne des Pyrénées Orientales. Ercynienne des Pyrénées Orientales. *Bulletin de la Société Géologique de France* **7**(4), 673–731.

Ayora, C. & Casas, J. M. (1983). Estudi microtermomètric dels filons de quars de les Esquerdes de Rojà, Massís de Canigó, Pirineu oriental. *Acta Geologica Hispanica* **18**, 35–46.

Ayora, C. & Casas, J. M. (1986). Strata-bound As-Au mineralization in pre-Caradocian rocks from the Vall de Ribes, eastern Pyrenees, Spain. *Mineralium Deposita* **21**, 278–287. https://doi.org/10.1007/BF00204346.

Ayora, C., Ribera, F. & Cardellach, E. (1992). The genesis of the arsenopyrite gold veins from the Vall de Ribes District, eastern Pyrenees, Spain. *Economic Geology* **87**, 1877–1896. https://doi.org/10.2113/gsecongeo.87.7.1877.

Bakker, R. J. & Elburg, M. A. (2006). A magmatic-hydrothermal transition in Arkaroola (northern Flinders ranges, South Australia): from diopside–titanite pegmatites to hematite–quartz growth. *Contributions to Mineralogy and Petrology* **152**, 541–569. https://doi.org/10.1007/s00410-006-0125-0.

Banerji, A. K. (1981). Ore genesis and its relationship to volcanism, tectonism, granitic activity, and metasomatism along the Singhbhum shear zone, eastern India. *Economic Geology* **76**, 905–912. https://doi.org/10.2113/gsecongeo.76.4.905.

Barbey, P. (2007). Diffusion-controlled biotite breakdown reaction textures at the solid/liquid transition in the continental crust. *Contributions to Mineralogy and Petrology* **154**, 707–716. https://doi.org/10.1007/s00410-007-0220-x.

Barth, N. C., Hacker, B. R., Seward, G. G. E. *et al.* (2010). Strain within the ultrahigh-pressure Western gneiss region of Norway recorded by quartz CPOs. *Geological Society, London, Special Publications* **335**, 663–685. https://doi.org/10.1144/SP335.27.

Bastin, E. S., Graton, L. C., Lindgren, W. *et al.* (1931). Criteria of age relations of minerals, with especial reference to polished sections of ores. *Economic Geology* **26**, 561–610. https://doi.org/10.2113/gsecongeo.26.6.561.

Benn, D., Martins, T. & Linnen, R. (2023). Fractionation and enrichment patterns in white mica from Li pegmatites of the Wekusko Lake pegmatite field, Manitoba, Canada. *The Canadian Mineralogist* **60**, 933–956. https://doi.org/10.3749/canmin.2200003.

Bons, P. D. (2000). The formation of veins and their microstructures. *Journal of the Virtual Explorer* **02**. https://doi.org/10.3809/jvirtex.2000.00007.

Bons, P. D. (2001). The formation of large quartz veins by rapid ascent of fluids in mobile hydrofractures. *Tectonophysics* **336**, 1–17. https://doi.org/10.1016/S0040-1951(01)00090-7.

Bons, P. D., Elburg, M. A. & Gomez-Rivas, E. (2012). A review of the formation of tectonic veins and their microstructures. *Journal of Structural Geology* **43**, 33–62. https://doi.org/10.1016/j.jsg.2012.07.005.

Bons, P. D., Cao, D., de Riese, T. *et al.* (2022). A review of natural hydrofractures in rocks. *Geological Magazine* **159**, 1–26. https://doi.org/10.1017/S0016756822001042.

Boulvais, P., Ruffet, G., Cornichet, J. & Mermet, M. (2007). Cretaceous albitization and dequartzification of Hercynian peraluminous granite in the Salvezines massif (French Pyrénées). *Lithos* **93**, 89–106.

Boutin, A., de Saint Blanquat, M., Poujol, M. *et al.* (2016). Succession of Permian and Mesozoic metasomatic events in the eastern Pyrenees with emphasis on the Trimouns talc–chlorite deposit. *International Journal of Earth Sciences (Geologische Rundschau)* **105**, 747–770. https://doi.org/10.1007/s00531-015-1223-x.

Cael, B. B., Heathcote, A. J. & Seekell, D. A. (2017). The volume and mean depth of Earth's lakes. *Geophysical Research Letters* **44**, 209–218. https://doi.org/10.1002/2016GL071378.

Canals, A., Van Driessche, A. E. S., Palero, F. & García-Ruiz, J. M. (2019). The origin of large gypsum crystals in the geode of Pulpí (Almería, Spain). *Geology* **47**, 1161–1165. https://doi.org/10.1130/G46734.1.

Cardellach, E., Ayora, C., Soler, A. & Delgado, J. (1992). The origin of fluids involved in the formation of gold-bearing skarns of the Andorra granite (Central Pyrenees, Spain): Sulphur isotope data. *Mineralogy and Petrology* **45**, 181–193. https://doi.org/10.1007/BF01163111.

Carmichael, D. M. (1987) Induced Stress and Secondary Mass Transfer: Thermodynamic Basis for the Tendency toward Constant-Volume Constraint in Diffusion Metasomatism. In: Helgeson H. C. (ed) *Chemical Transport in Metasomatic Processes*. Netherlands, Dordrecht: Springer, pp.239–264.

Casas, J. M. (1984) *Estudi de la deformació en els gneis del massís del Canigó*. PhD thesis. Universitat de Barcelona, unpublished, 284pp. Barcelona, Spain.

Casas, J.-M. (1986). Shear bands and related extensional structures in a mylonitized quartz dyke. *Journal of Structural Geology* **8**, 693–699. https://doi.org/10.1016/0191-8141(86)90074-X.

Casas, J. M. (2010). Ordovician deformations in the Pyrenees: new insights into the significance of pre-Variscan ('sardic') tectonics. *Geological Magazine* **147**, 674–689. https://doi.org/10.1017/S0016756809990756.

Casas, J. M., Castiñeiras, P., Navidad, M. *et al.* (2010). New insights into the late Ordovician magmatism in the eastern Pyrenees: U–Pb SHRIMP zircon data from the Canigó massif. *Gondwana Research* **17**, 317–324. https://doi.org/10.1016/j.gr.2009.10.006.

Casas, J. M., Navidad, M., Castiñeiras, P. *et al.* (2015). The late Neoproterozoic magmatism in the Ediacaran series of the eastern Pyrenees: new ages and isotope geochemistry. *International Journal of Earth Sciences (Geologische Rundschau)* **104**, 909–925. https://doi.org/10.1007/s00531-014-1127-1.

Casas, J. M., Álvaro, J. J., Clausen, S. *et al.* (2019) Palaeozoic Basement of the Pyrenees. In: Quesada C. & Oliveira J. T. (eds) *The Geology of Iberia: A Geodynamic Approach*. Cham: Springer International Publishing, pp.229–259.

Casas, J. M., Sánchez-García, T., Díez-Montes, A. *et al.* (2024). Extent and significance of the upper Ordovician felsic volcanism in the Pyrenees and Mouthoumet massifs, SW Europe. *Geological Society, London, Special Publications* **542**, SP542-2022-358. https://doi.org/10.1144/SP542-2022-358.

Castiñeiras, P., Navidad, M., Liesa, M. *et al.* (2008). U–Pb zircon ages (SHRIMP) for Cadomian and early Ordovician magmatism in the eastern Pyrenees: new insights into the pre-Variscan evolution of the northern Gondwana margin. *Tectonophysics* **461**, 228–239. https://doi.org/10.1016/j.tecto.2008.04.005.

Cavet, P. (1957). Le Paléozoïque de la zone axiale des Pyrénées orientales françaises entre le Roussillon et l'Andorre. *Bulletin Service Carte Géologique France* **55**, 303–309.

Charoy, B. & Pollard, P. J. (1989). Albite-rich, silica-depleted metasomatic rocks at Emuford, Northeast Queensland; mineralogical, geochemical, and fluid inclusion constraints on hydrothermal evolution and tin mineralization. *Economic Geology* **84**, 1850–1874. https://doi.org/10.2113/gsecongeo.84.7.1850.

Clarke, D. B. (1996). Two centuries after Hutton's theory of the earth': the status of granite science. *Transactions of the Royal Society of Edinburgh: Earth Sciences* **87**, 353–359.

Cocherie, A., Baudin, T., Autran, A. *et al.* (2005). U-Pb zircon (ID-TIMS and SHRIMP) evidence for the early ordovician intrusion of metagranites in the late Proterozoic Canaveilles Group of the Pyrenees and the Montagne noire (France). *Bulletin de la Société Géologique de France* **176**, 269–282. https://doi.org/10.2113/176.3.269.

Codeço, M. S., Weis, P., Trumbull, R. B. *et al.* (2021). The imprint of hydrothermal fluids on trace-element contents in white mica and tourmaline from the Panasqueira W–Sn–Cu deposit, Portugal. *Mineralium Deposita* **56**, 481–508. https://doi.org/10.1007/s00126-020-00984-8.

Cuney, M., Emetz, A., Mercadier, J. *et al.* (2012). Uranium deposits associated with Na-metasomatism from Central Ukraine: a review of some of the major deposits and genetic constraints. *Ore Geology Reviews* **44**, 82–106. https://doi.org/10.1016/j.oregeorev.2011.09.007.

Debon, F., Enrique, P. & Autran, A. (1996) Magmatisme Hercynian. In: Barnolas A. & Chiron J. C. (eds) *Synthèse géologique et géophysique des Pyrénées*, Vol. **1**, Introduction. Géophysique. Bureau de Recherches Géologiques et Minières - Instituto Tecnológico Geominero de España.

Denèle, Y., Laumonier, B., Paquette, J.-L. *et al.* (2014). Timing of granite emplacement, crustal flow and gneiss dome formation in the Variscan segment of the Pyrenees. *Geological Society, London, Special Publications* **405**, 265–287. https://doi.org/10.1144/SP405.5.

Dewers, T. & Ortoleva, P. J. (1989). Mechano-chemical coupling in stressed rocks. *Geochimica et Cosmochimica Acta* **53**, 1243–1258. https://doi.org/10.1016/0016-7037(89)90060-4.

Deymar, S., Yazdi, M., Rezvanianzadeh, M. R. & Behzadi, M. (2018). Alkali metasomatism as a process for Ti–REE–Y–U–Th mineralization in the Saghand anomaly 5, Central Iran: insights from geochemical, mineralogical, and stable isotope data. *Ore Geology Reviews* **93**, 308–336. https://doi.org/10.1016/j.oregeorev.2018.01.008.

Durney, D. W. & Ramsay, J. G. (1973) Incremental strains measured by syntectonic crystal growths. In: De Jong K. A. & Scholten R. (eds) *Gravity and tectonics*. NY: Wiley.

Dyck, B. & Larson, K. P. (2023). Metasomatic origin of the Himalayan banded tourmaline leucogranite. *Contributions to Mineralogy and Petrology* **178**, 37. https://doi.org/10.1007/s00410-023-02020-0.

Eggleton, R. A. & Banfield, J. F. (1985). The alteration of granitic biotite to chlorite. *American Mineralogist* **70**, 902–910.

Elburg, M. A., Bons, P. D., Dougherty-Page, J. *et al.* (2001). Age and metasomatic alteration of the Mt Neill granite at Nooldoonooldoona waterhole, Mt painter inlier, South Australia. *Australian Journal of Earth Sciences* **48**, 721–730. https://doi.org/10.1046/j.1440-0952.2001.485890.x.

Elburg, M. A., Andersen, T., Bons, P. D. *et al.* (2012). Metasomatism and metallogeny of A-type granites of the Mt painter–Mt Babbage inliers, South Australia. *Lithos* **151**, 83–104. https://doi.org/10.1016/j.lithos.2011.09.009.

Engvik, A. K., Putnis, A., Gerald, J. D. F. & Austrheim, H. (2008). Albitization of granitic rocks: the mechanism of replacement of oligoclase by albite. *The Canadian Mineralogist* **46**, 1401–1415. https://doi.org/10.3749/canmin.46.6.1401.

Espinola, M. R., Soler, A. & Arcos, D. (1996). Las mineralizaciones de wolframio asociadas a la granodiorita de Santa Coloma (Andorra). *Geogaceta* , 1586–1589.

Fàbrega, C., Parcerisa, D., Thiry, M. *et al.* (2012) Albitization profiles related to the Variscan basement, a case study of the Catalan Costal Ranges and the Eastern Pyrenees (NE Iberia). In: *International Conference Geofluids. "Abstract book. Geofluids VII International Conference"*, p. 103–107.

Fallourd, S., Poujol, M., Boulvais, P. *et al.* (2014). In situ LA-ICP-MS U–Pb titanite dating of Na–Ca metasomatism in orogenic belts: the north Pyrenean example. *International Journal of Earth Sciences (Geologische Rundschau)* **103**, 667–682. https://doi.org/10.1007/s00531-013-0978-1.

Finch, M. A., Bons, P. D., Steinbach, F. *et al.* (2020). The ephemeral development of C′ shear bands: a numerical modelling approach. *Journal of Structural Geology* **139**, 104091. https://doi.org/10.1016/j.jsg.2020.104091.

Fleet, M. E., Deer, W. A., Howie, R. A. & Zussman, J. (2003) *Rock-forming Minerals: Micas*. London (United Kingdom): Geological Society of London.

Fletcher, R. C. & Merino, E. (2001). Mineral growth in rocks: kinetic-rheological models of replacement, vein formation, and syntectonic crystallization. *Geochimica et Cosmochimica Acta* **65**, 3733–3748. https://doi.org/10.1016/S0016-7037(01)00726-8.

Fortuné, J. P. (1971) *Contribution à l'étude minéralogique et génétique des talcs Pyrénées*. Unpublished PhD thesis. Toulouse: Université Paul Sabatier, 454 p.

Gao, Y., Ye, H., Mao, J. & Li, Y. (2013). Geology, geochemistry and genesis of the Qianfanling quartz-vein Mo deposit in Songxian County, Western Henan Province, China. *Ore Geology Reviews* **55**, 13–28. https://doi.org/10.1016/j.oregeorev.2013.04.005.

Gisbert, G., Tornos, F., Losantos, E. *et al.* (2022). Vectors to ore in replacive volcanogenic massive sulphide deposits of the northern Iberian Pyrite Belt: major and trace element mineral chemistry. *Ore Geology Reviews* **147**, 104963. https://doi.org/10.1016/j.oregeorev.2022.104963.

Goncalves, P., Oliot, E., Marquer, D. & Connolly, J. A. D. (2012). Role of chemical processes on shear zone formation: an example from the Grimsel metagranodiorite (Aar massif, Central Alps). *Journal of Metamorphic Geology* **30**, 703–722. https://doi.org/10.1111/j.1525-1314.2012.00991.x.

González-Esvertit, E., Canals, À., Bons, P. D. *et al.* (2022a). Compiling regional structures in geological databases: the giant quartz veins of the Pyrenees as a case study. *Journal of Structural Geology* **163**, 104705. https://doi.org/10.1016/j.jsg.2022.104705.

González-Esvertit, E., Canals, À., Bons, P. D. *et al.* (2022b). Geology of giant quartz veins and their host rocks from the eastern Pyrenees (Southwest Europe). *Journal of Maps* **19**, 1–13. https://doi.org/10.1080/17445647.2022.2133642.

González-Esvertit, E., Molins-Vigatà, J., Canals, À. & Casas, J. M. (2023). The geology of the Gréixer area (La Cerdanya, eastern Pyrenees): Sardic, Variscan, and alpine imprints. *Trabajos de Geologia* **37**(37), 81–95. https://doi.org/10.17811/tdg.37.2023.81-95.

González-Esvertit, E., Canals, A., Bons, P. D. *et al.* (2024a). Chlorite chemical refinement during giant quartz vein formation. *GSA Bulletin* **136**, 5208–5216. https://doi.org/10.1130/B37510.1.

González-Esvertit, E., Canals, A., Prieto-Torrell, C. *et al.* (2024b) *NEIGRA - North-East Iberian Granitoids Database. Geochemistry of granitoids and orthogneisses from the Pyrenees and the Catalan Coastal Ranges [data set]*. Spain: DIGITAL.CSIC. http://doi.org/10.20350/DIGITALCSIC/16236.

González-Esvertit, E., Prieto-Torrell, C., Bons, P. D. *et al.* (2025a). A review of the granite concept through time. *Earth-Science Reviews* **261**, 105008. https://doi.org/10.1016/j.earscirev.2024.105008.

González-Esvertit, E., Fusswinkel, T., Canals, A. *et al.* (2025b). Fluid evolution and halogen fractionation in orogenic belts: a comparative fluid inclusion appraisal in the eastern Pyrenees. *Chemical Geology* **674**, 122578. https://doi.org/10.1016/j.chemgeo.2024.122578.

Grant, J. A. (1986). The isocon diagram; a simple solution to Gresens' equation for metasomatic alteration. *Economic Geology* **81**, 1976–1982. https://doi.org/10.2113/gsecongeo.81.8.1976.

Grant, J. A. (2005). Isocon analysis: a brief review of the method and applications. *Physics and Chemistry of the Earth, Parts A/B/C* **30**, 997–1004. https://doi.org/10.1016/j.pce.2004.11.003.

Graphchikov, A. A., Konilov, A. N. & Clemens, J. D. (1999). Biotite dehydration, partial melting, and fluid composition: experiments in the system KAlO2-FeO-MgO-SiO2-H2O-CO2. *American Mineralogist* **84**, 15–26. https://doi.org/10.2138/am-1999-1-202.

Gregory, D. D., Cracknell, M. J., Large, R. R. *et al.* (2019). Distinguishing ore deposit type and barren sedimentary pyrite using laser ablation-inductively coupled plasma-mass spectrometry trace element data and statistical analysis of Large data sets. *Economic Geology* **114**, 771–786. https://doi.org/10.5382/econgeo.4654.

Groves, D. I., Zhang, L. & Santosh, M. (2019). Subduction, mantle metasomatism, and gold: a dynamic and genetic conjunction. *GSA Bulletin* **132**, 1419–1426. https://doi.org/10.1130/B35379.1.

Gueydan, F., Leroy, Y. M., Jolivet, L. & Agard, P. (2003). Analysis of continental midcrustal strain localization induced by microfracturing and reaction-softening. *Journal of Geophysical Research: Solid Earth* **108**, 2064. https://doi.org/10.1029/2001JB000611.

Guidotti, C. V., Sassi, F. P., Blencoe, J. G. & Selverstone, J. (1994a). The paragonite-muscovite solvus: I. P-T-X limits derived from the Na-K compositions of natural, quasibinary paragonite-muscovite pairs. *Geochimica et Cosmochimica Acta* **58**, 2269–2275. https://doi.org/10.1016/0016-7037(94)90009-4.

Guidotti, C. V., Sassi, F. P., Sassi, R. & Blencoe, J. G. (1994b). The effects of ferromagnesian components on the paragonite-muscovite solvus: a semiquantitative analysis based on chemical data for natural paragonite-muscovite pairs. *Journal of Metamorphic Geology* **12**, 779–788. https://doi.org/10.1111/j.1525-1314.1994.tb00059.x.

Guitard, G. (1953). La structure du massif du Canigou; apercu Sur le metamorphisme regional dans la zone axiale des Pyrenees orientales (note preliminare) [with discussion]. *Bulletin de la Société Géologique de France* **S6-III**, 907–924.

Guitard, G. (1955). Sur l'evolution des gneiss des Pyrenees. *Bulletin de la Société Géologique de France* **S6-V**, 441–469. https://doi.org/10.2113/gssgfbull.S6-V.7-9.441.

Guitard, G. (1965) *Carte Géologique des Massifs du Canigou et de la Carançà à 1/50.000*. France: Bureau de Recherches Géologiques et Minières (BRGM), Service de la Carte Géologique de France.

Guitard G (1970) *Le métamorphisme hercynien mésozonal et les gneiss oeillés du massif du Canigou (Pyrénées orientales)*. *Mémoires du Bureau de Recherches Géologiques et Minières (BRGM)* **63**:353. France: BRGM

Guitard, G., Laumonier, B., Autran, A. *et al.* (1998a) *Notice explicative de la feuille Prades à 1/50,000*. Carte géologique par G. Guitard et al. (1992), Vol. **193**. France: BRGM Éditions-Service géologique national.

Guitard, G., Laumonier, B., Autran, A. *et al.* (1998b) *Notice explicative de la feuille Prats-de-Mollo-La-Preste à 1/50,000*, Vol. **193**. France: BRGM Éditions-Service géologique national.

Han, J., Hanchar, J. M., Pan, Y. *et al.* (2023). Hydrothermal alteration, not metamictization, is the main trigger for modifying zircon in highly evolved granites. *GSA Bulletin* **136**, 1878–1888. https://doi.org/10.1130/B36996.1.

Harlov, D. & Austrheim, H. (2012) *Metasomatism and the chemical transformation of rock: The role of fluids in terrestrial and extraterrestrial processes*. Berlin, Heidelberg: Springer; Springer Science & Business Media.

Hartevelt, J. A. A. (1970). Geology of the upper Segre and Valira valleys, Central Pyrenees, Andorra/Spain. *Leidse Geologische Mededelingen* **45**, 167–236.

Hayes, S. M. & McCullough, E. A. (2018). Critical minerals: a review of elemental trends in comprehensive criticality studies. *Resources Policy* **59**, 192–199. https://doi.org/10.1016/j.resourpol.2018.06.015.

Hecht, L., Thuro, K., Plinninger, R. & Cuney, M. (1999). Mineralogical and geochemical characteristics of hydrothermal alteration and episyenitization in the Königshain granites, northern bohemian massif, Germany. *International Journal of Earth Sciences* **88**, 236–252. https://doi.org/10.1007/s005310050262.

Heier, K. S. (1962). Trace elements in feldspars—a review. *Norsk Geologisk Tidsskrift* **42**, 415–454.

Hendry, D. A. F., Chivas, A. R., Long, J. V. P. & Reed, S. J. B. (1985). Chemical differences between minerals from mineralizing and barren intrusions from some north American porphyry copper deposits. *Contributions to Mineralogy and Petrology* **89**, 317–329. https://doi.org/10.1007/BF00381554.

Hilgers, C., Dilg-Gruschinski, K. & Urai, J. L. (2004). Microstructural evolution of syntaxial veins formed by advective flow. *Geology* **32**, 261–264. https://doi.org/10.1130/G20024.1.

Hirth, G. & Tullis, J. (1992). Dislocation creep regimes in quartz aggregates. *Journal of Structural Geology* **14**, 145–159. https://doi.org/10.1016/0191-8141(92)90053-Y.

Holness, M. B. (2003). Growth and albitization of K-feldspar in crystalline rocks in the shallow crust: a tracer for fluid circulation during exhumation? *Geofluids* **3**, 89–112.

de Hoÿm de Marien, L., Le Bayon, B., Pitra, P. *et al.* (2019). Two-stage Variscan metamorphism in the Canigou massif: evidence for crustal thickening in the Pyrenees. *Journal of Metamorphic Geology* **37**, 863–888. https://doi.org/10.1111/jmg.12487.

Hunter, N. J. R., Hasalová, P., Weinberg, R. F. & Wilson, C. J. L. (2016). Fabric controls on strain accommodation in naturally deformed mylonites: the influence of interconnected micaceous layers. *Journal of Structural Geology* **83**, 180–193. https://doi.org/10.1016/j.jsg.2015.12.005.

IGME (1972) *Mapa metalogenético 1:1.500.000*. Spain: Instituto Geológico y Minero de España (IGME).

IGME (1974) *Mapa Metalogenético de España a escala 1:200.000 (serie antigua)*. Spain: Instituto Geológico y Minero de España (IGME).

Imayama, T., Takeshita, T., Yi, K. & Fukuyama, M. (2019). Early Oligocene partial melting via biotite dehydration melting and prolonged low-pressure–low-temperature metamorphism of the upper high Himalaya crystalline sequence in the far east of Nepal. *Geological Society, London, Special Publications* **481**, 147–173. https://doi.org/10.1144/SP481.2.

Jamtveit, B., Putnis, C. V. & Malthe-Sørenssen, A. (2009). Reaction induced fracturing during replacement processes. *Contributions to Mineralogy and Petrology* **157**, 127–133. https://doi.org/10.1007/s00410-008-0324-y.

Jaques, L., Noronha, F., Liewig, N. & Bobos, I. (2016). Paleofluids circulation associated with the Gerês late-orogenic granitic massif, northern Portugal. *Geochemistry* **76**, 659–676. https://doi.org/10.1016/j.chemer.2016.09.006.

Jessell, M. W. (1987). Grain-boundary migration microstructures in a naturally deformed quartzite. *Journal of Structural Geology* **9**, 1007–1014. https://doi.org/10.1016/0191-8141(87)90008-3.

Jia, Y. & Kerrich, R. (2000). Giant quartz vein systems in accretionary orogenic belts: the evidence for a metamorphic £uid origin from N15N and N13C studies. *Earth and Planetary Science Letters* **84**, 211–224.

Kelemen, P. B. & Hirth, G. (2012). Reaction-driven cracking during retrograde metamorphism: olivine hydration and carbonation. *Earth and Planetary Science Letters* **345–348**, 81–89. https://doi.org/10.1016/j.epsl.2012.06.018.

Koehn, D., Arnold, J. & Passchier, C. W. (2005). Fracture and vein patterns as indicators of deformation history: a numerical study. *Geological Society, London, Special Publications* **243**, 11–24. https://doi.org/10.1144/GSL.SP.2005.243.01.03.

Lacroix, A. (1896). Les transformations endomorphiques du magma granitique dans la haute ariege, au contact des calcaires. *Comptes Rendus de l'Académie des sciences France* **123**, 1021–1023.

Lacroix, A. (1898) *Le granite des Pyrénées et ses phénomènes de contact* Bull. Carte Gdol. France, 64. Paris (France): Librairie polytechnique.

Lacroix, M. A. (1920). Les roches éruptives du Crétace pyrénéen et la nomenclature des roches éruptives modifiées. *Comptes Rendues Acad Sci France* **170**, 685–690.

Laumonier, B. (1988). Les groupes de Canaveilles et de Jujols ('"Paléozoïque inférieur"') des Pyrénées orientales – arguments en faveur de l'âge essentiellement Cambrien de ces séries. *Hercynica* **4**, 25–38.

Laumonier, B., Calvet, M., Bayon, B. L. & Barbey, P. (2015) *Notice explicative de la feuille Prats-de-Mollo-La-Preste à 1/50,000*, Vol. **193**. BRGM Éditions-Service géologique national. France: Bureau de Recherches Géologiques et Minières.

van der Leeden, F., Troise, F. & Todd, D. K. (1990) *The Water Encyclopedia, Second Edition*, 2nd edn. Chelsea, Mich: CRC Press.

Lehnert, K., Su, Y., Langmuir, C. H. *et al.* (2000). A global geochemical database structure for rocks. *Geochemistry, Geophysics, Geosystems* **1**. https://doi.org/10.1029/1999GC000026.

Lemarchand, J., Boulvais, P., Gaboriau, M. *et al.* (2012). Giant quartz vein formation and high-elevation meteoric fluid infiltration into the south Armorican shear zone: geological, fluid inclusion and stable isotope evidence. *Journal of the Geological Society* **169**, 17–27. https://doi.org/10.1144/0016-76492010-186.

Lemirre, B., Cochelin, B., Duchene, S. *et al.* (2019). Origin and duration of late orogenic magmatism in the foreland of the Variscan belt (Lesponne — Chiroulet — Neouvielle area, French Pyrenees). *Lithos* **336–337**, 183–201. https://doi.org/10.1016/j.lithos.2019.03.037.

Liesa, M. & Carreras, J. (1989). On the structure and metamorphism of the roc de Frausa massif (eastern Pyrenees). *Geodinamica Acta* **3**, 149–161. https://doi.org/10.1080/09853111.1989.11105182.

Liesa, M., Casas, J. M., Castiñeiras, P. *et al.* (2008) Correlation of Late Neoproterozoic sequences of the Eastern Pyrenees based on U-Pb (SHRIMP) zircon data. In: *Geo-Temas*. Spain: Sociedad Geológica de España, pp.701–704.

Liesa, M., Aguilar, C., Castro, A. *et al.* (2021). The role of mantle and crust in the generation of calc-alkaline Variscan magmatism and its tectonic setting in the eastern Pyrenees. *Lithos* **406–407**, 106541. https://doi.org/10.1016/j.lithos.2021.106541.

Lindgren, W. (1925). Gel replacement, a new aspect of metasomatism. *Proceedings of the National Academy of Sciences of the United States of America* **11**, 5–11. https://doi.org/10.1073/pnas.11.1.5.

Link, G., Vanderhaeghe, O., Béziat, D. *et al.* (2020) Thermal peak detected in gold-bearing shear zones by a thermo-structural study: a new tool to retrieve fluid flow? In: *15th SGA Biennal Meeting on Life with Ore Deposits on Earth*. United States: Geological Society of America, pp.260–263.

López-Moro, F. J., Moro, M. C., Timón, S. M. *et al.* (2013). Constraints regarding gold deposition in episyenites: the Permian episyenites associated with the Villalcampo shear zone, central western Spain. *International Journal of Earth Sciences (Geologische Rundschau)* **102**, 721–744. https://doi.org/10.1007/s00531-012-0844-6.

Maggi, M., Rossetti, F., Ranalli, G. & Theye, T. (2014). Feedback between fluid infiltration and rheology along a regional ductile-to-brittle shear zone: the east Tenda shear zone (alpine Corsica). *Tectonics* **33**, 253–280. https://doi.org/10.1002/2013TC003370.

Maliva, R. G. & Siever, R. (1988). Diagenetic replacement controlled by force of crystallization. *Geology* **16**, 688–691. https://doi.org/10.1130/0091-7613(1988)016<0688:DRCBFO>2.3.CO;2.

Marsala, A. & Wagner, T. (2016). Mass transfer and fluid evolution in late-metamorphic veins, Rhenish massif (Germany): insight from alteration geochemistry and fluid-mineral equilibria modeling. *Mineralogy and Petrology* **110**, 515–545. https://doi.org/10.1007/s00710-016-0424-8.

Martín-Closas, C., Trias, S. & Casas, J. M. (2018). New palaeobotanical data from carboniferous culm deposits constrain the age of the Variscan deformation in the eastern Pyrenees. *Geologica Acta* **16**, 107–123. https://doi.org/10.1344/GeologicaActa2018.16.2.1.

Martínez, F. J., Iriondo, A., Dietsch, C. *et al.* (2011). U-Pb SHRIMP-RG zircon ages and Nd signature of lower Paleozoic rifting-related magmatism in the Variscan basement of the eastern Pyrenees. *Lithos* **127**, 10–23. https://doi.org/10.1016/j.lithos.2011.08.004.

Matter, J. M., Stute, M., Snæbjörnsdottir, S. Ó. *et al.* (2016). Rapid carbon mineralization for permanent disposal of anthropogenic carbon dioxide emissions. *Science* **352**, 1312–1314.

McNab, R. R., Brugger, J., Voisey, C. R. *et al.* (2024). Coprecipitation of amorphous silica and gold nanoparticles contributes to gold hyperenrichment. *Geology* **52**(10), 737–741.

Menegon, L., Pennacchioni, G. & Spiess, R. (2008). Dissolution-precipitation creep of K-feldspar in mid-crustal granite mylonites. *Journal of Structural Geology* **30**, 565–579. https://doi.org/10.1016/j.jsg.2008.02.001.

Merino, E. (2017) Mineral replacement and dynamics of metasomatism: The blind spot of geochemists as illustrated by the brucite-for-periclase replacement in magnesian marbles. In: *15th Water-Rock Interaction International Symposium, WRI-15*.

Merino, E. & Canals, À. (2011) Self-accelerating dolomite-for-calcite replacement: Self-organized dynamics of burial dolomitization and associated mineralization. *American Journal of Science* **311**, 573–607. https://doi.org/10.2475/07.2011.01.

Miller, S. A. (2013) Chapter 1 - The Role of Fluids in Tectonic and Earthquake Processes. *Advances in Geophysics* **54**, 1–46. https://doi.org/10.1016/B978-0-12-380940-7.00001-9.

Mishra, B., Pruseth, K. L., Hazarika, P. & Chinnasamy, S. S. (2018). Nature and source of the ore-forming fluids associated with orogenic gold deposits in the Dharwar craton. *Geoscience Frontiers* **9**, 715–726. https://doi.org/10.1016/j.gsf.2017.09.005.

Moncada, D., Mutchler, S., Nieto, A. *et al.* (2012). Mineral textures and fluid inclusion petrography of the epithermal Ag–Au deposits at Guanajuato, Mexico: application to exploration. *Journal of Geochemical Exploration* **114**, 20–35. https://doi.org/10.1016/j.gexplo.2011.12.001.

Moore, D. E. & Liou, J. G. (1979). Chessboard-twinned albite from Franciscan metaconglomerates of the diablo range, California. *American Mineralogist* **64**, 329–336.

Morozova, L., Zozulya, D., Selivanova, E. *et al.* (2022). Distribution of trace elements in K-feldspar with implications for tracing ore-forming processes in pegmatites: examples from the world-class Kolmozero lithium deposit, NW Russia. *Minerals* **12**, 1448. https://doi.org/10.3390/min12111448.

Muñoz, J. A. (1992) Evolution of a continental collision belt: ECORS-Pyrenees crustal balanced cross-section. In: McClay K. R. (ed) *Thrust Tectonics*. Dordrecht: Springer Netherlands, pp.235–246.

Muñoz, J. A. (2019) Alpine Orogeny: Deformation and Structure in the Northern Iberian Margin (Pyrenees s.l.). In: Quesada C. & Oliveira J. T. (eds) *The Geology of Iberia: A Geodynamic Approach*. Cham: Springer International Publishing, pp.433–451.

Munoz, M., Baron, S., Boucher, A. *et al.* (2016). Mesozoic vein-type Pb–Zn mineralization in the Pyrenees: Lead isotopic and fluid inclusion evidence from the les Argentières and Lacore deposits. *Comptes Rendus Geoscience* **348**, 322–332. https://doi.org/10.1016/j.crte.2015.07.001.

Nahon, D. & Merino, E. (1997). Pseudomorphic replacement in tropical weathering; evidence, geochemical consequences, and kinetic-rheological origin. *American Journal of Science* **297**, 393–417. https://doi.org/10.2475/ajs.297.4.393.

Navidad, M., Castiñeiras, P., Casas, J. M. *et al.* (2018). Ordovician magmatism in the eastern Pyrenees: implications for the geodynamic evolution of northern Gondwana. *Lithos* **314–315**, 479–496. https://doi.org/10.1016/j.lithos.2018.06.019.

Nijland, T. G. & Touret, J. L. R. (2001). Replacement of graphic pegmatite by graphic albite-actinolite-clinopyroxene intergrowths (Mjåvatn, southern Norway). *European Journal of Mineralogy* **13**, 41–50. https://doi.org/10.1127/0935-1221/01/0013-0041.

Nishimoto, S. & Yoshida, H. (2010). Hydrothermal alteration of deep fractured granite: effects of dissolution and precipitation. *Lithos* **115**, 153–162. https://doi.org/10.1016/j.lithos.2009.11.015.

Nishimoto, S., Yoshida, H., Asahara, Y. *et al.* (2014). Episyenite formation in the Toki granite, Central Japan. *Contributions to Mineralogy and Petrology* **167**, 960. https://doi.org/10.1007/s00410-013-0960-8.

O'Hara, K. (1988). Fluid flow and volume loss during mylonitization: an origin for phyllonite in an overthrust setting, North Carolina U.S.a. *Tectonophysics* **156**, 21–36. https://doi.org/10.1016/0040-1951(88)90280-6.

Oberthür, T., Weiser, T., Amanor, J. A. & Chryssoulis, S. L. (1997). Mineralogical siting and distribution of gold in quartz veins and sulfide ores of the Ashanti mine and other deposits in the Ashanti belt of Ghana: genetic implications. *Mineralium Deposita* **32**, 2–15. https://doi.org/10.1007/s001260050068.

Odlum, M. L. & Stockli, D. F. (2020). Geochronologic constraints on deformation and metasomatism along an exhumed mylonitic shear zone using apatite U-Pb, geochemistry, and microtextural analysis. *Earth and Planetary Science Letters* **538**, 116177. https://doi.org/10.1016/j.epsl.2020.116177.

Odlum, M. L., Levy, D. A., Stockli, D. F. *et al.* (2022). Deformation and metasomatism recorded by single-grain apatite petrochronology. *Geology* **50**, 697–703. https://doi.org/10.1130/G49809.1.

Padel, M., Clausen, S., Álvaro, J. J. & Casas, J. M. (2018). Review of the Ediacaran-lower Ordovician (pre-Sardic) stratigraphic framework of the eastern Pyrenees, southwestern Europe. *Geologica Acta* **16**, 339–365.

Padel, M., Clausen, S., Poujol, M. & Álvaro, J. J. (2022). Shifts in the Ediacaran to lower Ordovician sedimentary zircon provenances of Northwest Gondwana: the Pyrenean files. *Geologica Acta* **20**, 1–18.

Pan, L., Carter, J., Quantin-Nataf, C. *et al.* (2021). Voluminous silica precipitated from Martian waters during late-stage aqueous alteration. *Planetary Science Journal* **2**, 65. https://doi.org/10.3847/PSJ/abe541.

Passchier, C. W. & Trouw, R. A. J. (1996) *Microtectonics*. Berlin: Springer Verlag.

Pati, J. K., Patel, S. C., Pruseth, K. L. *et al.* (2007). Geology and geochemistry of giant quartz veins from the Bundelkhand craton, Central India and their implications. *Journal of Earth System Science* **116**, 497–510.

Pedrosa, E., Putnis, C. V., Renard, F. *et al.* (2016). Porosity generated during the fluid-mediated replacement of calcite by fluorite. *CrystEngComm* **18**, 6867–6874. https://doi.org/10.1039/C6CE01150K.

Pennacchioni, G., Ceccato, A., Fioretti, A. M. *et al.* (2016). Episyenites in meta-granitoids of the Tauern window (eastern Alps): unpredictable? *Journal of Geodynamics* **101**, 73–87. https://doi.org/10.1016/j.jog.2016.04.001.

Petersson, J. & Eliasson, T. (1997). Mineral evolution and element mobility during episyenitization (dequartzification) and albitization in the postkinematic Bohus granite, Southwest Sweden. *Lithos* **42**, 123–146. https://doi.org/10.1016/S0024-4937(97)00040-6.

Petersson, J., Stephens, M. B., Mattsson, H. & Möller, C. (2012). Albitization and quartz dissolution in Paleoproterozoic metagranite, Central Sweden — implications for the disposal of spent nuclear fuel in a deep geological repository. *Lithos* **148**, 10–26. https://doi.org/10.1016/j.lithos.2012.06.001.

Plümper, O., Botan, A., Los, C. *et al.* (2017). Fluid-driven metamorphism of the continental crust governed by nanoscale fluid flow. *Nature Geoscience* **10**, 685–690. https://doi.org/10.1038/ngeo3009.

Plümper, O., Wallis, D., Teuling, F. *et al.* (2022). High-magnitude stresses induced by mineral-hydration reactions. *Geology* **50**, 1351–1355. https://doi.org/10.1130/G50493.1.

Poitrenaud, T., Poujol, M., Augier, R. & Marcoux, E. (2020). The polyphase evolution of a late Variscan W/Au deposit (Salau, French Pyrenees): insights from REE and U/Pb LA-ICP-MS analyses. *Mineralium Deposita* **55**, 1127–1147. https://doi.org/10.1007/s00126-019-00923-2.

Polizzi, S. (1990) *Les minéralisations sulfo-arséniées aurifères du massif des Aspres (Pyrénées orientales, France) : étude géologique et métallogénique*. Unpublished PhD thesis, Université Paul Sabatier, Toulouse (France).

Poujol, M., Boulvais, P. & Kosler, J. (2010). Regional-scale cretaceous albitization in the Pyrenees: evidence from *in situ* U–Th–Pb dating of monazite, titanite and zircon. *Journal of the Geological Society* **167**, 751–767. https://doi.org/10.1144/0016-76492009-144.

Puddu, C., Álvaro, J. J., Carrera, N. & Casas, J. M. (2019). Deciphering the Sardic (Ordovician) and Variscan deformations in the eastern Pyrenees, SW Europe. *Journal of the Geological Society* **176**, 1191–1206. https://doi.org/10.1144/jgs2019-057.

Pujol-Solà, N., Casas, J. M., Proenza, J. A. *et al.* (2022). Cadomian metabasites of the eastern Pyrenees revisited. *Geologica Acta* **I–IV**, 1–26.

Putnis, A. (2009). Mineral replacement reactions. *Reviews in Mineralogy and Geochemistry* **70**, 87–124. https://doi.org/10.2138/rmg.2009.70.3.

Putnis, A. & Austrheim, H. (2010). Fluid-induced processes: metasomatism and metamorphism. *Geofluids* **10**, 254–269. https://doi.org/10.1111/j.1468-8123.2010.00285.x.

Quesnel, B., Boiron, M.-C., Cathelineau, M. *et al.* (2019). Nature and origin of mineralizing fluids in Hyperextensional systems: the case of cretaceous Mg metasomatism in the Pyrenees. *Geofluids* **2019**, e7213050. https://doi.org/10.1155/2019/7213050.

Ramsay, J. G. (1980). The crack–seal mechanism of rock deformation. *Nature* **284**, 135–139. https://doi.org/10.1038/284135a0.

Read, H. H. (1957) *The Granite Controversy*. London: Thomas Murby.

Ren, M. (2004). Partitioning of Sr, Ba, Rb, Y, and LREE between alkali feldspar and peraluminous silicic magma. *American Mineralogist* **89**, 1290–1303. https://doi.org/10.2138/am-2004-8-918.

Roberts, M. P., Pin, C., Clemens, J. D. & Paquette, J.-L. (2000). Petrogenesis of mafic to felsic plutonic rock associations: the calc-alkaline Quérigut complex, French Pyrenees. *Journal of Petrology* **41**, 809–844.

Roest, W. R. & Srivastava, S. P. (1991). Kinematics of the plate boundaries between Eurasia, Iberia, and Africa in the North Atlantic from the late cretaceous to the present. *Geology* **19**, 613–616. https://doi.org/10.1130/0091-7613(1991)019<0613:KOTPBB>2.3.CO;2.

Rosenbaum, G., Lister, G. S. & Duboz, C. (2002). Relative motions of Africa, Iberia and Europe during alpine orogeny. *Tectonophysics* **359**, 117–129. https://doi.org/10.1016/S0040-1951(02)00442-0.

Rout, D., Panigrahi, M. K., Mernagh, T. P. & Pati, J. K. (2022). Origin of the Paleoproterozoic "Giant quartz reef" system in the Bundelkhand craton, India: constraints from fluid inclusion microthermometry, Raman spectroscopy, and geochemical modelling. *Lithosphere* **2022**, 3899542. https://doi.org/10.2113/2022/3899542.

Rutherford, M. J. (1969). An experimental determination of iron biotite-alkali feldspar equilibria. *Journal of Petrology* **10**, 381–408. https://doi.org/10.1093/petrology/10.3.381.

Saishu, H., Okamoto, A. & Otsubo, M. (2017). Silica precipitation potentially controls earthquake recurrence in seismogenic zones. *Scientific Reports* **7**, 13337. https://doi.org/10.1038/s41598-017-13597-5.

Santanach, P. (1972a). Estudio tectónico del Paleozoico inferior del Pirineo entre la Cerdaña y el río Ter. *Acta Geologica Hispanica* **7**, 44–49.

Santanach, P. (1972b). Sobre una discordancia en el Paleozoico inferior de los Pirineos orientales. *Acta Geologica Hispanica* **7**, 129–132.

Schandl, E. S. & Gorton, M. P. (2012). Hydrothermal alteration and CO2 metasomatism (natural carbon sequestration) of komatiites in the South-Western Abitibi greenstone belt. *The Canadian Mineralogist* **50**, 129–146. https://doi.org/10.3749/canmin.50.1.129.

Schärer, Parseval, D., Polvé & Blanquat, D. S. (1999). Formation of the Trimouns talc-chlorite deposit (Pyrenees) from persistent hydrothermal activity between 112 and 97 ma. *Terra Nova* **11**, 30–37. https://doi.org/10.1046/j.1365-3121.1999.00224.x.

Schmid, S. M. & Casey, M. (1986) Complete Fabric Analysis of Some Commonly Observed Quartz C-Axis Patterns. In: *Mineral and Rock Deformation*. United States: American Geophysical Union (AGU), pp.263–286. https://doi.org/10.1029/GM036p0263.

Seedorff, E., Dilles, J. H., Proffett, J. M., Jr. *et al.* (2005) Porphyry Deposits: Characteristics and Origin of Hypogene Features. In: Hedenquist J. W., JFH T., Goldfarb R. J. & Richards J. P. (eds) *One Hundredth Anniversary Volume*. United States: Society of Economic Geologists.

Sharp, Z. D., Masson, H. & Lucchini, R. (2005). Stable isotope geochemistry and formation mechanisms of quartz veins; extreme paleoaltitudes of the Central Alps in the Neogene. *American Journal of Science* **305**, 187–219. https://doi.org/10.2475/ajs.305.3.187.

Shaw, D. M. (1952). The geochemistry of thallium. *Geochimica et Cosmochimica Acta* **2**, 118–154. https://doi.org/10.1016/0016-7037(52)90003-3.

Sibson, R. H. (1977). Fault rocks and fault mechanisms. *Journal of the Geological Society* **133**, 191–213. https://doi.org/10.1144/gsjgs.133.3.0191.

Sibson, R. H. (2020). Preparation zones for large crustal earthquakes consequent on fault-valve action. *Earth, Planets and Space* **72**, 31. https://doi.org/10.1186/s40623-020-01153-x.

Sibson, R. H., Moore, J. M. M. & Rankin, A. H. (1975). Seismic pumping—a hydrothermal fluid transport mechanism. *Journal of the Geological Society* **131**, 653–659. https://doi.org/10.1144/gsjgs.131.6.0653.

Sillitoe, R. H. (2002). Some metallogenic features of gold and copper deposits related to alkaline rocks and consequences for exploration. *Mineralium Deposita* **37**, 4–13. https://doi.org/10.1007/s00126-001-0227-6.

Sillitoe, R. H. (2010). Porphyry copper systems. *Economic Geology* **105**, 3–41. https://doi.org/10.2113/gsecongeo.105.1.3.

Simpson, C. (1985). Deformation of granitic rocks across the brittle-ductile transition. *Journal of Structural Geology* **7**, 503–511.

Slabunov, A. I. & Singh, V. K. (2022). Giant quartz veins of the Bundelkhand craton, Indian shield: new geological data and U-Th-Pb age. *Minerals* **12**, 168. https://doi.org/10.3390/min12020168.

Soler, A. (1990) *Geologia i metallogenia de la terminacio sud del granit d'Andorra (Pirineu Central)*. Unpublished PhD thesis. Barcelona: Univ. de Barcelona.

Soler, A. & Enrique, P. (1989). La terminación Sur-occidental del batolito de Andorra-Mont LLluís: características petrológicas y geoquímicas. *Acta Geológica Hispánica* **24**, 139–146.

Soltani Dehnavi, A., McFarlane, C. R. M., Lentz, D. R. *et al.* (2019). Chlorite-white mica pairs' composition as a micro-chemical guide to fingerprint massive sulfide deposits of the Bathurst mining camp, Canada. *Minerals* **9**, 125. https://doi.org/10.3390/min9020125.

Stanley, C. R. (2020). Molar element ratio analysis of lithogeochemical data: a toolbox for use in mineral exploration and mining. *Geochemistry: Exploration, Environment, Analysis* **20**, 233–256. https://doi.org/10.1144/geochem2019-033.

Staude, S., Bons, P. D. & Markl, G. (2009). Hydrothermal vein formation by extension-driven dewatering of the middle crust: an example from SW Germany. *Earth and Planetary Science Letters* **286**, 387–395. https://doi.org/10.1016/j.epsl.2009.07.012.

Stipp, M., Stünitz, H., Heilbronner, R. & Schmid, S. M. (2002). Dynamic recrystallization of quartz: correlation between natural and experimental conditions. *Geological Society, London, Special Publications* **200**, 171–190. https://doi.org/10.1144/GSL.SP.2001.200.01.11.

Suikkanen, E. & Rämö, O. T. (2019). Episyenites—characteristics, genetic constraints, and mineral potential. *Mining, Metallurgy & Exploration* **36**, 861–878. https://doi.org/10.1007/s42461-019-00120-9.

Tajčmanová, L., Vrijmoed, J. & Moulas, E. (2015). Grain-scale pressure variations in metamorphic rocks: implications for the interpretation of petrographic observations. *Lithos* **216–217**, 338–351. https://doi.org/10.1016/j.lithos.2015.01.006.

Tanner, P. W. G. (2012). The giant quartz-breccia veins of the Tyndrum–Dalmally area, Grampian highlands, Scotland: their geometry, origin and relationship to the Cononish gold–silver deposit. *Earth and Environmental Science Transactions of the Royal Society of Edinburgh* **103**, 51–76. https://doi.org/10.1017/S1755691012000084.

Tannock, L., Herwegh, M., Berger, A. *et al.* (2020). Microstructural analyses of a giant quartz reef in South China reveal episodic brittle-ductile fluid transfer. *Journal of Structural Geology* **130**, 103911. https://doi.org/10.1016/j.jsg.2019.103911.

Tischendorf, G., Förster, H.-J., Gottesmann, B. & Rieder, M. (2007). True and brittle micas: composition and solid-solution series. *Mineralogical Magazine* **71**, 285–320. https://doi.org/10.1180/minmag.2007.071.3.285.

Tokle, L., Hirth, G. & Stünitz, H. (2023). The effect of muscovite on the microstructural evolution and rheology of quartzite in general shear. *Journal of Structural Geology* **169**, 104835. https://doi.org/10.1016/j.jsg.2023.104835.

Toy, V. G., Prior, D. J. & Norris, R. J. (2008). Quartz fabrics in the alpine fault mylonites: influence of pre-existing preferred orientations on fabric development during progressive uplift. *Journal of Structural Geology* **30**, 602–621. https://doi.org/10.1016/j.jsg.2008.01.001.

Tulloch, A. J. (1979). Secondary Ca-Al silicates as low-grade alteration products of granitoid biotite. *Contributions to Mineralogy and Petrology* **69**, 105–117. https://doi.org/10.1007/BF00371854.

U.S. Geological Survey, Department of the Interior. (2022). 2022 Final List of Critical Minerals. In: *Federal Register*. United States. https://www.federalregister.gov/documents/2022/02/24/2022-04027/2022-final-list-of-critical-minerals. Accessed 22 Sep 2023. Internal Report.

Vilà, M., Pin, C., Enrique, P. & Liesa, M. (2005). Telescoping of three distinct magmatic suites in an orogenic setting: generation of Hercynian igneous rocks of the Albera massif (eastern Pyrenees). *Lithos* **83**, 97–127.

Voll, G. (1976). Recrystallization of quartz, biotite and feldspars from Erstfeld to the Leventina nappe, Swiss Alps, and its geological significance. *Schweizerische Mineralogische und Petrographische Mitteilungen* **56**, 641–647.

Wang, H., van Hunen, J. & Pearson, D. G. (2015). The thinning of subcontinental lithosphere: the roles of plume impact and metasomatic weakening. *Geochemistry, Geophysics, Geosystems* **16**, 1156–1171. https://doi.org/10.1002/2015GC005784.

Warr, L. N. (2021). IMA–CNMNC approved mineral symbols. *Mineralogical Magazine* **85**, 291–320. https://doi.org/10.1180/mgm.2021.43.

Weber, J., Cheshire, M. C., Bleuel, M. *et al.* (2021). Influence of microstructure on replacement and porosity generation during experimental dolomitization of limestones. *Geochimica et Cosmochimica Acta* **303**, 137–158. https://doi.org/10.1016/j.gca.2021.03.029.

Weisheit, A., Bons, P. D. & Elburg, M. A. (2013). Long-lived crustal-scale fluid flow: the hydrothermal mega-breccia of Hidden Valley, Mt. painter inlier, South Australia. *International Journal of Earth Sciences (Geologische Rundschau)* **102**, 1219–1236. https://doi.org/10.1007/s00531-013-0875-7.

Wenker, S. & Beaumont, C. (2018). Can metasomatic weakening result in the rifting of cratons? *Tectonophysics* **746**, 3–21. https://doi.org/10.1016/j.tecto.2017.06.013.

Wilkinson, M. D., Dumontier, M., Aalbersberg, I. J. *et al.* (2016). The FAIR guiding principles for scientific data management and stewardship. *Scientific Data* **3**, 160018. https://doi.org/10.1038/sdata.2016.18.

Williams, R. T. & Fagereng, Å. (2022). The role of quartz cementation in the seismic cycle: a critical review. *Reviews of Geophysics* **60**, e2021RG000768. https://doi.org/10.1029/2021RG000768.

Wilshire, H. G. (1984). Mantle metasomatism: the REE story. *Geology* **12**, 395–398. https://doi.org/10.1130/0091-7613(1984)12<395:MMTRS>2.0.CO;2.

Wintsch, R. P. & Yi, K. (2002). Dissolution and replacement creep: a significant deformation mechanism in mid-crustal rocks. *Journal of Structural Geology* **24**, 1179–1193. https://doi.org/10.1016/S0191-8141(01)00100-6.

Yardley, B. W. D. (1983). Quartz veins and devolatilization during metamorphism. *Journal of the Geological Society* **140**, 657–663. https://doi.org/10.1144/gsjgs.140.4.0657.

Zharikov, V. A., Pertsev, N. N., Rusinov, V. L. *et al.* (2007) *Metasomatism and metasomatic rocks. A classification of metamorphic rocks and glossary of terms*. Recommendations of the International Union of Geological Sciences Subcommission on the Systematics of Metamorphic Rocks. International Union of Geological Sciences (IUGS).

Zwart, H. J. (1986). The variscan geology of the Pyrenees. *Tectonophysics* **129**, 9–27. https://doi.org/10.1016/0040-1951(86)90243-X.

Journal of Petrology, 2025, **66**, egaf007
https://doi.org/10.1093/petrology/egaf007
Original Manuscript